

# AGN feedback in the Local Universe: multiphase outflow of the Seyfert galaxy NGC 5506

Federico Esposito<sup>1,2</sup>, Almudena Alonso-Herrero<sup>3</sup>, Santiago García-Burillo<sup>4</sup>, Viviana Casasola<sup>5</sup>, Françoise Combes<sup>6</sup>, Daniele Dallacasa<sup>1,5</sup>, Richard Davies<sup>7</sup>, Ismael García-Bernete<sup>8</sup>, Begoña García-Lorenzo<sup>9,10</sup>, Laura Hermosa Muñoz<sup>3</sup>, Luis Peralta de Arriba<sup>3</sup>, Miguel Pereira-Santaella<sup>11</sup>, Francesca Pozzi<sup>1,2</sup>, Cristina Ramos Almeida<sup>9,10</sup>, Thomas Taro Shimizu<sup>7</sup>, Livia Vallini<sup>2</sup>, Enrica Bellocchi<sup>12,13</sup>, Omaira González-Martín<sup>14</sup>, Erin K. S. Hicks<sup>15</sup>, Sebastian Hönig<sup>16</sup>, Alvaro Labiano<sup>17</sup>, Nancy A. Levenson<sup>18</sup>, Claudio Ricci<sup>19,20</sup>, and David J. Rosario<sup>21</sup>

<sup>1</sup> Dipartimento di Fisica e Astronomia, Università degli Studi di Bologna, Via P. Gobetti 93/2, I-40129 Bologna, Italy  
e-mail: federico.esposito7@unibo.it

<sup>2</sup> Osservatorio di Astrofisica e Scienza dello Spazio (INAF–OAS), Via P. Gobetti 93/3, I-40129 Bologna, Italy

<sup>3</sup> Centro de Astrobiología (CAB), CSIC-INTA, Camino Bajo del Castillo s/n, E-28692 Villanueva de la Cañada, Madrid, Spain

<sup>4</sup> Observatorio de Madrid, OAN-IGN, Alfonso XII, 3, E-28014 Madrid, Spain

<sup>5</sup> INAF – Istituto di Radioastronomia, Via P. Gobetti 101, 40129, Bologna, Italy

<sup>6</sup> Observatoire de Paris, LERMA, Collège de France, CNRS, PSL University, Sorbonne University, 75014, Paris

<sup>7</sup> Max-Planck-Institut für Extraterrestrische Physik (MPE), Giessenbachstraße 1, D-85748 Garching, Germany

<sup>8</sup> Department of Physics, University of Oxford, Keble Road, Oxford OX1 3RH, UK

<sup>9</sup> Instituto de Astrofísica de Canarias (IAC), Calle Vía Láctea, s/n, 38205 La Laguna, Tenerife, Spain

<sup>10</sup> Departamento de Astrofísica, Universidad de La Laguna, 38206 La Laguna, Tenerife, Spain

<sup>11</sup> Instituto de Física Fundamental, CSIC, Calle Serrano 123, 28006 Madrid, Spain

<sup>12</sup> Departamento de Física de la Tierra y Astrofísica, Fac. de CC Físicas, Universidad Complutense de Madrid, 28040 Madrid, Spain

<sup>13</sup> Instituto de Física de Partículas y del Cosmos IPARCOS, Fac. de CC Físicas, Universidad Complutense de Madrid, 28040 Madrid, Spain

<sup>14</sup> Instituto de Radioastronomía and Astrofísica (IRyA-UNAM), 3-72 (Xangari), 8701, Morelia, Mexico

<sup>15</sup> Department of Physics & Astronomy, University of Alaska Anchorage, AK 99508-4664, USA

<sup>16</sup> Department of Physics & Astronomy, University of Southampton, Hampshire, SO17 1BJ, Southampton, UK

<sup>17</sup> Telespazio UK for the European Space Agency (ESA), ESAC, Camino Bajo del Castillo s/n, 28692 Villanueva de la Cañada, Spain

<sup>18</sup> Space Telescope Science Institute, 3700 San Martin Drive, Baltimore, Maryland 21218, USA

<sup>19</sup> Instituto de Estudios Astrofísicos, Facultad de Ingeniería y Ciencias, Universidad Diego Portales, Avenida Ejercito Libertador 441, Santiago, Chile

<sup>20</sup> Kavli Institute for Astronomy and Astrophysics, Peking University, Beijing 100871, China

<sup>21</sup> School of Mathematics, Statistics and Physics, Newcastle University, Newcastle upon Tyne, NE1 7RU, UK

Received XXX; accepted YYY

## ABSTRACT

We present new optical GTC/MEGARA seeing-limited (0.9'') integral-field observations of NGC 5506, together with ALMA observations of the CO(3 – 2) transition at a 0.2'' (~ 25 pc) resolution. NGC 5506 is a luminous (bolometric luminosity of ~ 10<sup>44</sup> erg s<sup>-1</sup>) nearby (26 Mpc) Seyfert galaxy, part of the Galaxy Activity, Torus, and Outflow Survey (GATOS). We modelled the CO(3 – 2) kinematics with <sup>3D</sup>BAROLO, revealing a rotating and outflowing cold gas ring within the central 1.2 kpc. We derived an integrated cold molecular gas mass outflow rate for the ring of ~ 8 M<sub>⊙</sub> yr<sup>-1</sup>. We fitted the optical emission lines with a maximum of two Gaussian components to separate rotation from non-circular motions. We detected high [OIII]λ5007 projected velocities (up to ~ 1000 km s<sup>-1</sup>) at the active galactic nucleus (AGN) position, decreasing with radius to an average ~ 330 km s<sup>-1</sup> around ~ 350 pc. We also modelled the [OIII] gas kinematics with a non-parametric method, estimating the ionisation parameter and electron density in every spaxel, from which we derived an ionised mass outflow rate of 0.076 M<sub>⊙</sub> yr<sup>-1</sup> within the central 1.2 kpc. Regions of high CO(3 – 2) velocity dispersion, extending to projected distances of ~ 350 pc from the AGN, appear to be the result from the interaction of the AGN wind with molecular gas in the galaxy's disc. Additionally, we find the ionised outflow to spatially correlate with radio and soft X-ray emission in the central kiloparsec. We conclude that the effects of AGN feedback in NGC 5506 manifest as a large-scale ionised wind interacting with the molecular disc, resulting in outflows extending to radial distances of 610 pc.

**Key words.** galaxies: individual: NGC 5506 – galaxies: active – galaxies: Seyfert – ISM: jets and outflows – ISM: kinematics and dynamics

## 1. Introduction

The feedback from active galactic nuclei (AGN) has been proposed as a key mechanism influencing the course of galaxy

evolution (see e.g. the reviews by Alexander & Hickox 2012; Fabian 2012; Kormendy & Ho 2013; Heckman & Best 2014; Harrison et al. 2018). AGN are powered by supermassive black

holes (SMBHs) and their accretion discs located at galactic centres, emitting intense radiation and influencing the excitation and kinematics of the surrounding gas. This feedback process initiates from a very small region ( $10^{-3}$  pc is a typical accretion disc radius, see [Cornachione et al. 2020](#); [Guo et al. 2022](#); [Jha et al. 2022](#)), yet its effects can extend to influence the entire galaxy structure ([Okamoto et al. 2005](#); [Croton et al. 2006](#); [Gaibler et al. 2012](#); [McNamara & Nulsen 2012](#); [Feruglio et al. 2015](#); [Dubois et al. 2016](#); [Anglés-Alcázar et al. 2017](#)).

Analysing AGN feedback is a complex task due to its impact on different phases of the interstellar medium (ISM) across different physical scales, from the sub-parsec highly ionised ultrafast outflows (UFOs, [Tombesi et al. 2010](#); [Fukumura et al. 2015](#); [Nomura et al. 2016](#)), warm absorbers ([Blustin et al. 2005](#); [Laha et al. 2014](#)), and broad absorption lines (BALs, [Weymann et al. 1991](#); [Proga et al. 2000](#)), to the kiloparsec-scale ionised ([McCarthy et al. 1996](#); [Baum & McCarthy 2000](#); [Liu et al. 2013](#); [Perna et al. 2020](#); [Fluetsch et al. 2021](#)) and molecular ([Feruglio et al. 2010](#); [Cicone et al. 2014](#); [Bischetti et al. 2019](#); [Ramos Almeida et al. 2022](#)) outflows, up to the megaparsec-scale emission of giant radio galaxies (GRGs, [Ishwara-Chandra & Saikia 1999](#); [Kuźmierz et al. 2018](#); [Dabhade et al. 2020](#)) and X-ray groups and clusters ([McCarthy et al. 2010](#); [Fabian et al. 2011](#); [McNamara & Nulsen 2012](#); [Pasini et al. 2020](#)).

Furthermore, AGN activity is considered to be intermittent over the course of a galaxy's lifetime ([King et al. 2004](#); [Hopkins & Hernquist 2006](#); [Schawinski et al. 2015](#); [King & Nixon 2015](#)), or even on timescales of days or less ([Dultzin-Hacyan et al. 1992](#); [Wagner & Witzel 1995](#)). Consequently, comprehending the overall impact of AGN feedback is highly challenging, requiring the use of multiwavelength, multi-scale, and multi-time observations as essential tools.

The molecular phase of the ISM is of paramount importance, since it is the fuel for star formation and the phase in which the bulk of the gaseous mass in star-forming galaxies resides (e.g. [Casasola et al. 2020](#)). The AGN radiation heats the molecular gas by creating X-ray-dominated regions within the ISM ([Maloney et al. 1996](#); [Esposito et al. 2022, 2024](#); [Wolfire et al. 2022](#)), and it perturbs its kinematics, driving outflows ([Cicone et al. 2014](#); [Fiore et al. 2017](#); [Veilleux et al. 2020](#); [Lamperti et al. 2022](#)).

Molecular gas typically forms a rotating disc associated with the galaxy gravitational potential. In AGN-host galaxies, a common form of perturbation involves the interaction between the molecular disc and the AGN hot wind, which manifests as outflowing ionised gas observable in X-rays ([Cappi 2006](#); [Tombesi et al. 2013](#); [Giustini et al. 2023](#)), UV ([Hewett & Foltz 2003](#); [Rankine et al. 2020](#)) and optical ([Fabian 2012](#); [Mullaney et al. 2013](#)) wavelengths (see also the review by [Veilleux et al. 2020](#), and references therein, for the hot-cold gas coupling). In this regard, a multiwavelength approach is essential to effectively trace the multiphase outflow ([Davies et al. 2014](#); [Cicone et al. 2018](#); [García-Bernete et al. 2021](#); [Speranza et al. 2024](#)). Nearby AGN serve as a perfect laboratory for studying these feedback signatures in detail, particularly with the increasingly improved spatial resolution and spectral coverage of today's instruments.

The Galactic Activity, Torus, and Outflow Survey (GATOS) aims to understand the obscuring material (torus) and the nuclear gas cycle (inflows and outflows) in the immediate surroundings of the nuclear region of local AGN ([García-Burillo et al. 2021](#); [Alonso-Herrero et al. 2021](#); [García-Bernete et al. 2024](#)). The GATOS sample includes Seyfert galaxies with distances 10 – 40 Mpc, selected from the 70-month Burst Alert Telescope (BAT) catalogue of AGN ([Baumgartner et al. 2013](#)), some of which have been observed at different wavelengths, including optical

and near-infrared integral field unit (IFU) spectroscopy, JWST, and ALMA observations.

One of the key findings of the GATOS survey is the existence of an anti-correlation between the nuclear molecular gas concentration and the AGN power: for a sample of 18 galaxies ([García-Burillo et al. 2021](#)) and an extended sample ([García-Burillo et al.](#), in preparation). Molecular gas, traced by low- $J$  CO lines and observed by ALMA at a spatial resolution  $\sim 10$  pc, is also detected in outflows in those sources showing the most extreme nuclear-scale gas deficiencies, hence suggesting that the AGN power plays a role in clearing the nuclear region. These outflows have been observed and analysed in detail for some GATOS selected sources, which have been analysed in detail for the molecular and ionised phases ([Alonso-Herrero et al. 2018, 2019, 2023](#); [García-Bernete et al. 2021](#); [Peralta de Arriba et al. 2023](#)).

In this study, we investigate the molecular and ionised gas phases of NGC 5506, an Sa spiral galaxy in the GATOS sample at a redshift-independent distance of 26 Mpc ([Karachentsev et al. 2006](#)). At this distance the spatial scale is 125 pc $''$ . NGC 5506 has an AGN bolometric luminosity of  $\sim 1.3 \times 10^{44}$  erg s $^{-1}$  ([Davies et al. 2014](#)) and is classified as an optically obscured narrow line Seyfert 1 (NLSy1, [Nagar et al. 2002](#)). The black hole mass is  $M_{\text{BH}} = 2.0^{+8.0}_{-1.6} \times 10^7 M_{\odot}$  ([Gofford et al. 2015](#)), yielding an Eddington ratio of  $\lambda_{\text{Edd}} \equiv L_{\text{bol}}/L_{\text{Edd}} = 0.05^{+0.21}_{-0.04}$ . NGC 5506 is notable in the GATOS sample for having one of the highest molecular gas nuclear deficiencies (see Fig. 18 of [García-Burillo et al. 2021](#)), suggesting a potential imprint of AGN feedback on the molecular gas. Furthermore, NGC 5506 hosts a sub-parsec bent radio jet ([Roy et al. 2000, 2001](#); [Kinney et al. 2000](#)) and a UFO ([Gofford et al. 2013, 2015](#)), making it an intriguing target for investigating multiphase (and multiscale) outflows. As a NLSy1, NGC 5506 is expected to be in a young AGN phase, characterised by a small black hole mass and a high accretion rate (see e.g. [Crenshaw et al. 2003](#); [Tarchi et al. 2011](#); [Salomé et al. 2023](#)).

Evidence of complex kinematics from the long-slit optical spectrum was found by [Wilson et al. \(1985\)](#), who suggested radial motion for the ionised gas. [Maiolino et al. \(1994\)](#) refined this model, identifying outflowing velocities of up to 400 km s $^{-1}$  for [OIII], [NII], and H $\alpha$ , with the outflow cone inclined at  $-15^{\circ}$  from the north. Additionally, [Fischer et al. \(2013\)](#) estimated an ionised outflow velocity of 500 km s $^{-1}$  using slitless *Hubble* Space Telescope (HST) observations (see also [Ruiz et al. 2005](#)), modelling a biconical outflow. [Davies et al. \(2020\)](#) carried out a detailed analysis of optical data from observations made with X-shooter at VLT, finding a [OIII] outflow with a maximum velocity of 792 km s $^{-1}$  and  $\dot{M}_{\text{out}} = 0.21 M_{\odot} \text{ yr}^{-1}$ . [Riffel et al. \(2017, 2021\)](#) and [Bianchin et al. \(2022\)](#) studied the outflow of the ionised gas in the near-IR (with GEMINI NIFS), finding a mass outflow rate ranging from 0.11 to 12.49  $M_{\odot} \text{ yr}^{-1}$  (by adopting two fixed  $n_e$  values - 500 cm $^{-3}$  and 10 $^4$  cm $^{-3}$  - and exploring different geometries). The highest outflow values would result in a kinetic efficiency  $\dot{E}_{\text{out}}/L_{\text{bol}} = 0.71$ . They also calculate, from  $L_{\text{bol}}$ , a mass accretion rate to the SMBH of 0.067  $M_{\odot} \text{ yr}^{-1}$ .

In this work, we present new IFU observations made with the Multi-Espectrógrafo en GTC de Alta Resolución para Astronomía (MEGARA) at the Gran Telescopio Canarias (GTC), which cover several optical emission lines, together with ALMA Band 7 observations of the CO(3 – 2) transition. The paper is structured as follows. In Section 2 we present the ALMA Band 7 and GTC/MEGARA observations. In Section 3 we describe the morphology of the molecular and ionised gas emission lines, while we model the kinematics of the two phases in Sections 4 and 5, respectively. In Section 6 we discuss the results of this

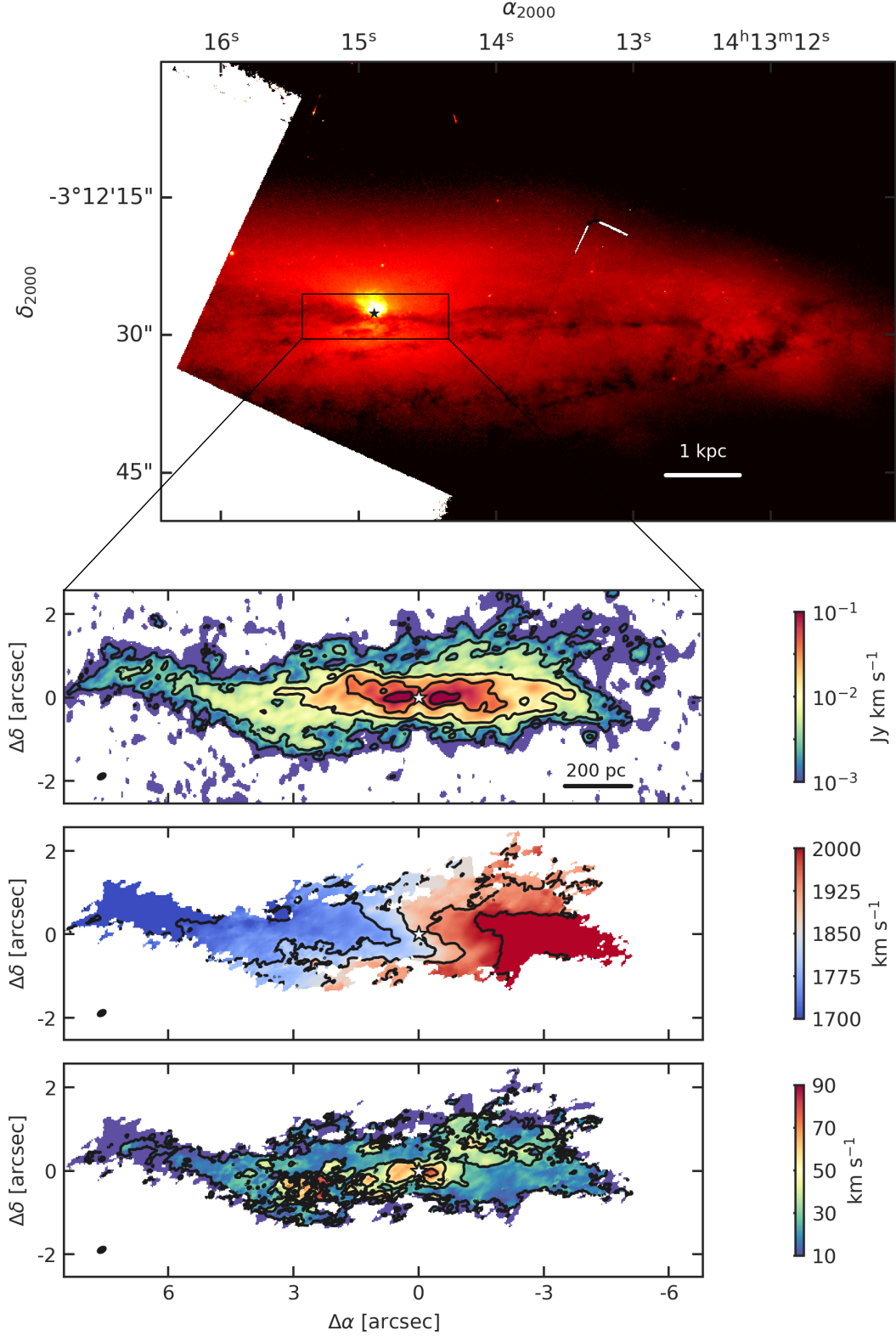


**Fig. 1.** Optical and molecular views of NGC 5506. *Top.* HST/F606W image of NGC 5506 from [Malkan et al. \(1998\)](#). The black rectangle identifies a region of  $15.3'' \times 5.1''$  (corresponding to  $1.9 \times 0.6 \text{ kpc}^2$ ). *Bottom.* ALMA CO(3 – 2) intensity, velocity and velocity dispersion maps, clipped at a signal-to-noise ratio of 3. The contours are between  $10^{-3}$  and  $10^{-1} \text{ Jy km s}^{-1}$  (with 0.5 dex steps) for the intensity map, between 1700 and 2000  $\text{km s}^{-1}$  (with 75  $\text{km s}^{-1}$  steps) for the velocity map, and between 10 and 90  $\text{km s}^{-1}$  (with 20  $\text{km s}^{-1}$  steps) for the velocity dispersion map. North is up and east is left, and offsets in the ALMA maps are measured relative to the  $870 \mu\text{m}$  continuum peak (as in [García-Burillo et al. 2021](#)), marked with a star symbol in every panel. The ALMA beam ( $0.21'' \times 0.13''$ ) appears in every bottom panel as a black ellipse in the lower left.

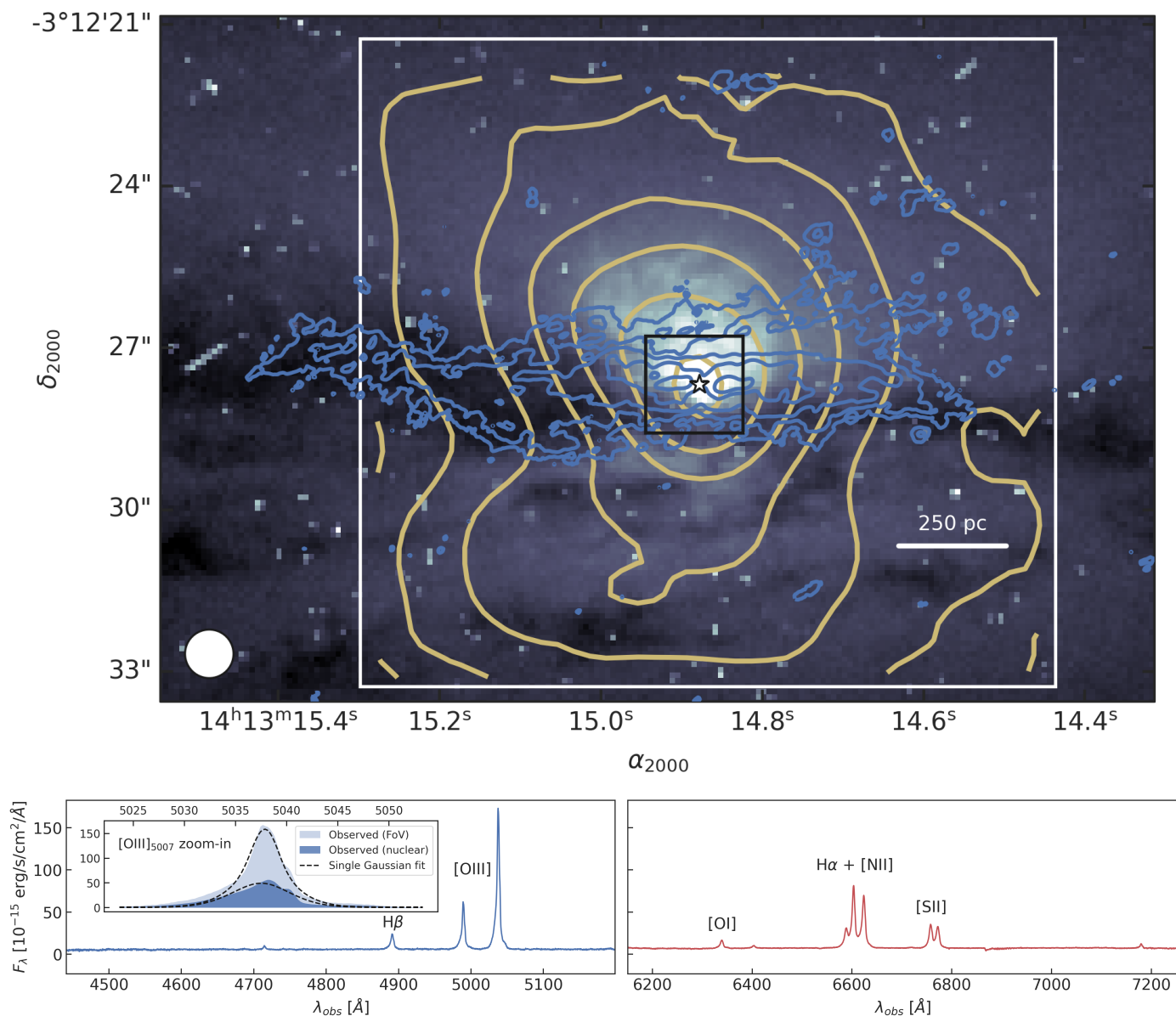


**Fig. 2.** Optical image and spectra of the central region of NGC 5506. *Top.* GTC/MEGARA [OIII] ( $\lambda_e = 5007 \text{ \AA}$ , in orange) and CO ( $\lambda_e = 870 \mu\text{m}$ , in blue) contours over the HST/F606W image of NGC 5506 (Malkan et al. 1998). The [OIII] contour levels, from the single-component Gaussian fit, have a logarithmic spacing from  $3\sigma$  to 80% of the peak intensity in steps of 0.5 dex, while the CO(3 – 2) contours are the same of Fig. 1. The white star symbol is the AGN position, as determined in Section 2.2. The black and white squares are the nuclear region, with size  $1.8 \text{ arcsec} \sim 225 \text{ pc}$ , observed by X-shooter (see Davies et al. 2020), and the MEGARA FoV ( $12.5'' \times 11.3'' \sim 1.5 \text{ kpc} \times 1.4 \text{ kpc}$ ), respectively. The white circle in the bottom left is the MEGARA seeing conditions (diameter  $0.9''$ ). *Bottom.* Left and right panels contain the spectra (integrated within the MEGARA FoV) revealed with the MEGARA LR-B and LR-R gratings, respectively, with names of identified emission lines and doublets. The inset is the zoom-in of a [OIII] line (after continuum subtraction): the blue shadings are the observed spectra of the MEGARA FoV and of the nuclear region, the black dashed lines are the fits with a single Gaussian. The inset axes have the same units of the outer panel.

work and we compare our data with the available literature, and we draw our conclusions in Section 7.

## 2. Observations

### 2.1. ALMA Band 7

We observed NGC 5506 with the Band 7 ALMA receiver and a single pointing (project-ID: #2017.1.00082.S; PI: S. García-Burillo). We analysed the moderate resolution datacube from García-Burillo et al. (2021). The datacube has a  $0.21'' \times 0.13''$  ( $26 \text{ pc} \times 16 \text{ pc}$ ) beam (with PA =  $-60^\circ$ , measured anticlock-

wise from the northern direction), a  $17''$  (2.1 kpc) field of view (FoV) and a largest angular scale of  $4''$  (0.5 kpc). To check the astrometry, we first aligned the HST/F606W image (top panel of Fig. 1) with the position of stars (from the Gaia mission), and then we aligned the ALMA continuum peak and the HST peak, resulting in  $\alpha_{2000} = 14^{\text{h}}13^{\text{m}}14.877^{\text{s}}$ ,  $\delta_{2000} = -03^\circ 12' 27.67''$  (as in García-Burillo et al. 2021).

### 2.2. GTC/MEGARA Bands B and R

We observed the central region of NGC 5506 on 20/03/2021 (Program GTC27-19B; PI: A. Alonso-Herrero), with MEGARA

**Table 1.** Fundamental parameters for NGC 5506.

Parameter	Value	Reference <sup>a</sup>
$\alpha_{2000}$	14 <sup>h</sup> 13 <sup>m</sup> 14.877 <sup>s</sup>	(1)
$\delta_{2000}$	-03°12'27.67"	(1)
$V_{\text{hel}}^{\text{b}}$	1882 ± 11 km s <sup>-1</sup>	(1)
RC3 Type	Sa pec edge-on	(2)
Nuclear activity	Optically obscured NLSy1	(3)
Distance	26 Mpc (1'' = 125 pc)	(4)
$D_{25}$	2.82'	(5)
Inclination	80°	(1)
Position Angle	265°	(1)
$M_{\text{BH}}$	2.0 <sup>+8.0</sup> <sub>-1.6</sub> × 10 <sup>7</sup> M <sub>⊙</sub>	(6)
$L_{\text{bol}}$	1.3 × 10 <sup>44</sup> erg s <sup>-1</sup>	(7)
$L_{\text{IR}}$	3.1 × 10 <sup>10</sup> L <sub>⊙</sub>	(8)
$\lambda_{\text{Edd}}$	0.05 <sup>+0.21</sup> <sub>-0.04</sub>	(1)

**Notes.** <sup>a</sup> (1) This paper; (2) de Vaucouleurs et al. (1991); (3) Nagar et al. (2002); (4) Karachentsev et al. (2006); (5) Baillard et al. (2011); (6) Gofford et al. (2015); (7) Davies et al. (2020); (8) Sanders et al. (2003). <sup>b</sup> Heliocentric velocity is the mean between the systemic velocities derived for the molecular and the ionised gas

in IFU mode (Gil de Paz et al. 2016; Carrasco et al. 2018). We used two low resolution (LR) volume phase holographic gratings: the LR-B (spectral range ~ 4300 – 5200 Å, resolution  $R \sim 5000$ ), to observe H $\beta$  and the [OIII] $\lambda\lambda$ 4959, 5007 doublet (exposure time 480 s), and the LR-R (~ 6100 – 7300 Å,  $R \sim 5900$ ), to observe H $\alpha$ , [OI] $\lambda$ 6300, and the [NII] $\lambda\lambda$ 6548, 6583 and [SII] $\lambda\lambda$ 6716, 6731 doublets (exposure time 400 s). The observed FoV is 12.5'' × 11.3'', corresponding to 1.6 × 1.4 kpc<sup>2</sup>.

The data reduction was performed by following Peralta de Arriba et al. (2023) and using the official MEGARA pipeline (Pascual et al. 2021). The resolution of the GTC/MEGARA observations was limited by the seeing conditions. We plotted it with a circle of diameter 0.9'' in all the relevant figures. The final datacubes were produced with a spaxel size of 0.3'', as recommended by the pipeline developers (Pascual et al. 2021; Peralta de Arriba et al. 2023): this corresponds to a physical spaxel size of 37.5 pc. We corrected the maps astrometry from the two configurations by aligning their continuum peaks with the ALMA Band 7 (870  $\mu$ m) and HST (F606W filter) ones; to this point as the AGN position. We note that optical extinction may have an impact on the observed optical nucleus and actual AGN location on scales below the MEGARA seeing of 0.9''.

### 3. Morphology and kinematics

#### 3.1. ALMA CO(3-2)

Fig. 1 shows the Hubble Space Telescope (HST) image and the ALMA CO(3 – 2) first three moments maps. The CO intensity map reveals an edge-on disc with a nuclear deficit (with respect to the circumnuclear region) of diameter ~ 100 pc. This molecular gas depletion in the very centre has already been observed and analysed in García-Burillo et al. (2021). The circumnuclear disc is symmetric up to a diameter of ~ 7'' = 875 pc. At radii larger than 3 – 4'' there is an extended gas tail in the eastern direction, which traces the dust lane visible in the HST image (see also Fig. 2).

The bottom panels of Fig. 1 show the velocity and velocity dispersion of CO(3 – 2). The velocity field is centred at 1850

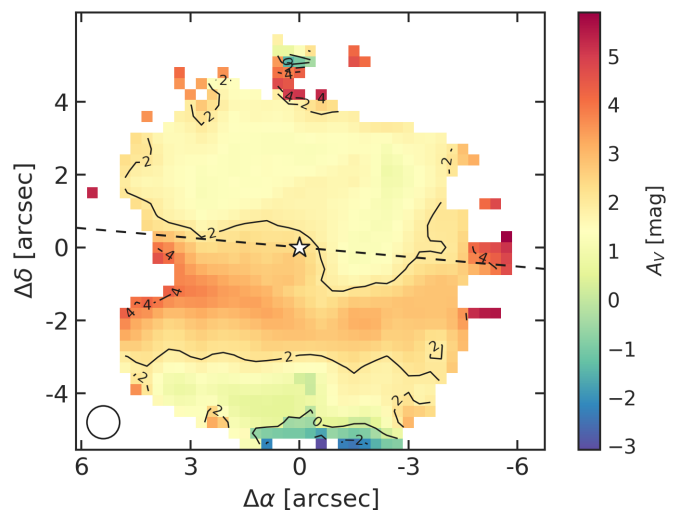


**Fig. 3.** Visual extinction map of the MEGARA FoV, calculated from the H $\alpha$ /H $\beta$  ratio and with  $R_V = 3.1$  (Cardelli et al. 1989). The white star symbol is the AGN position, and distances are relative to it. The dashed black line is our fiducial major kinematic axis with PA = 265° (see Section 4). The white circle in the bottom left is the MEGARA seeing conditions.

km s<sup>-1</sup>. It appears to be dominated by rotation, redshifted on the western side and blueshifted on the eastern side. However, it also exhibits perturbations due to non-circular motion. The velocity dispersion has a median value of 17 km s<sup>-1</sup>, and displays higher values along the NW-SE axis, with a maximum value of 86 km s<sup>-1</sup> at  $\delta\alpha \sim 3''$ .

#### 3.2. GTC/MEGARA emission lines

To derive the line intensity and kinematics, we extracted and fitted every spaxel of the MEGARA FoV with the ALUCINE<sup>1</sup> (Ajuste de Líneas para Unidades de Campo Integral de Nebulosas en Emisión, Peralta de Arriba et al. 2023), initially with a single Gaussian and an amplitude-over-noise (AoN) of 3 or higher. Fig. 2 shows the contours of the [OIII] doublet intensity, which are the brightest lines in the MEGARA spectrum (also in Fig. 2). The other identified emission lines, namely H $\beta$ , [OI], H $\alpha$  + [NII] doublet, and [SII] doublet, are labelled in Fig. 2.

The [OIII] emission of Fig. 2 nicely follows the HST image, and it is shaped as a bicone, typical of narrow line regions (NLRs Pogge 1988; Wilson et al. 1993; Schmitt et al. 2003). The bicone emerges almost vertically in projection from the dusty molecular disc (~ 20° anticlockwise from the north, as reported by Fischer et al. 2013; García-Burillo et al. 2021). We note here that Fischer et al. (2013) detected a one-sided ionisation cone (the northern side) using slitless spectroscopy of the [OIII] line. This is also evident in the HST map (Figs. 1 and 2). With MEGARA we detect the southern side as well, although it appears more extinguished. To check this we derived, following Cardelli et al. (1989), the visual extinction map from the H $\alpha$ /H $\beta$  line ratios (whereas the line fluxes come from the single Gaussian fit spaxel-by-spaxel). The resulting map (Fig. 3) shows a clear dust band crossing the southern side of NGC 5506 nuclear region. This piece of information also suggests that the southern side is the near side of the galaxy (in accordance with García-Burillo et al. 2021, analysis).

<sup>1</sup> Available at [https://gitlab.com/lperalta\\_ast/alucine](https://gitlab.com/lperalta_ast/alucine)

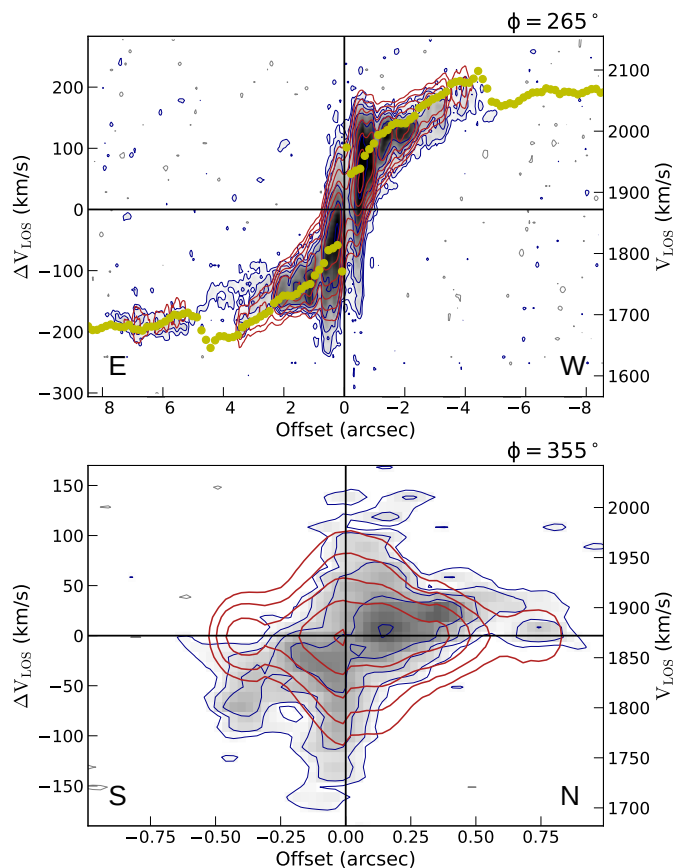


**Fig. 4.** ALMA CO(3 – 2) PV diagrams generated with 3DB along the kinematic major (*top panel*) and minor (*bottom panel*) axes. The grey scale and blue contours are the ALMA CO(3 – 2) observations  $> 3\sigma$ , while the red contours are the 3DB rotating disc model (without a radial velocity component). The yellow dots are the fitted rotation curve. The approximate eastern, western, southern, and northern directions are marked in the panels.

It is tempting to interpret the comparison of [OIII] and CO contours in Fig. 2 as an ionised outflow that escapes the galaxy disc following the path of less resistance (Faucher-Giguère & Quataert 2012). We explore this possibility in Section 6.

#### 4. Modelling the molecular gas kinematics

The CO(3 – 2) velocity field map (Fig. 1) shows the typical signatures of a rotating disc with some deviations from non-circular motions. We modelled the CO(3 – 2) datacube with  $3\text{DBAROLO}^2$  (Di Teodoro & Fraternali 2015, hereafter 3DB), which creates a disc model for the rotating gas by dividing the emission into concentric rings, and fits the following parameters for every ring: the kinematic centre coordinates, the scale-height of the disc ( $z_0$ ), the inclination ( $i$ ) of the disc with respect to the line of sight, the position angle (PA, measured anticlockwise from the northern direction for the receding side of the rotating disc) of the major kinematic axis, the systemic velocity  $v_{\text{sys}}$  with which the whole galaxy is receding from us, the rotational velocity ( $v_{\text{rot}}$ ) of the gas, the velocity dispersion ( $\sigma_{\text{gas}}$ ), and the radial velocity ( $v_{\text{rad}}$ ).

We note here that 3DB is designed to model the gas kinematics within a rotating disc (plus a radial velocity component). Our strategy is to use 3DB to identify and quantify any radial

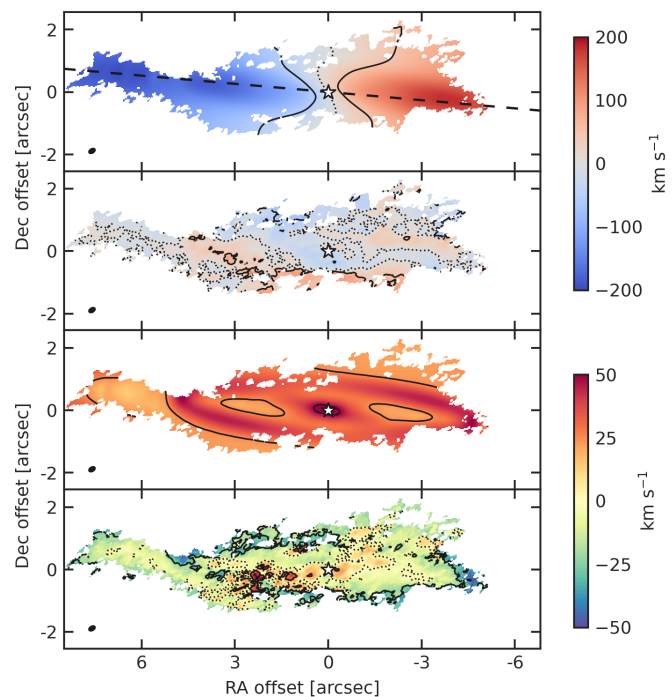


**Fig. 5.** Best-fit model and residuals (i.e. observation minus the model) obtained with 3DB for the rotating disc with a radial velocity component. Top and bottom panels show the mean velocity field and the velocity dispersion field of CO(3 – 2), respectively. In the first panel,  $v_{\text{sys}} = 1872 \text{ km s}^{-1}$  has been subtracted from the model velocities. Velocity contours (top panels) are at  $-50$  and  $50 \text{ km s}^{-1}$  (solid) and at  $0 \text{ km s}^{-1}$  (dotted), while dispersion contours (bottom panels) are at  $-50$ ,  $-25$ ,  $25$ , and  $50 \text{ km s}^{-1}$  (solid) and at  $0 \text{ km s}^{-1}$  (dotted). The dashed black line in the first panel is the kinematic major axis with PA =  $265^\circ$ . The ALMA beam appears in every panel as a black ellipse in the bottom left.

motion within the disc, which may point to an inflow or outflow of gas. If the radial flow forms an angle  $\theta_{\text{out}}$  with the galaxy disc, only the velocity projected on the disc, that is,  $v_{\text{out}} \cos \theta_{\text{out}}$ , will be detected by 3DB (see also Di Teodoro & Peek 2021; Bacchini et al. 2023).

We fixed the kinematic centre at the position of the continuum peak. We set a ring radial size of  $0.15''$  ( $\approx 19 \text{ pc}$ ), similar to the ALMA beam ( $0.21'' \times 0.13''$ ), and a total of 60 rings, thus reaching out to a distance of  $9''$  ( $\approx 1.1 \text{ kpc}$ ) from the centre.

##### 4.1. Rotating disc

We performed a first 3DB run with  $v_{\text{rad}} = 0 \text{ km s}^{-1}$ , and  $z_0$ ,  $i$ , PA,  $v_{\text{sys}}$ ,  $v_{\text{rot}}$ , and  $\sigma_{\text{gas}}$  as free parameters. In this way we derived  $z_0 = 0.2'' \approx 25 \text{ pc}$ ,  $i = 80^\circ$ , PA =  $265^\circ$ , and  $v_{\text{sys}} = 1872 \pm 10 \text{ km s}^{-1}$  (where the error is given by the ALMA datacube spectral step). The inclination is the same as that found by García-Burillo et al. (2021) with the software kinemetry (Krajnović et al. 2006), while the PA is slightly different (they found PA =  $275^\circ$ ). The  $v_{\text{sys}}$  value is in agreement with several works: Fischer et al. (2013) reported  $1823 \text{ km s}^{-1}$ , Riffel et al. (2017)  $1878 \text{ km s}^{-1}$ , Davies et al. (2020)  $1962 \text{ km s}^{-1}$ , García-Burillo et al. (2021)  $1840 \text{ km s}^{-1}$ , and the average of these values is  $1876 \text{ km s}^{-1}$ , only  $4 \text{ km s}^{-1}$  over our estimate.

We then performed a 3DB run with  $v_{\text{rot}}$  and  $\sigma_{\text{gas}}$  as the only free parameters, while the others were fixed to the values determined in the first run. This approach assumes the absence of

<sup>2</sup> Available at <https://bbarolo.readthedocs.io>

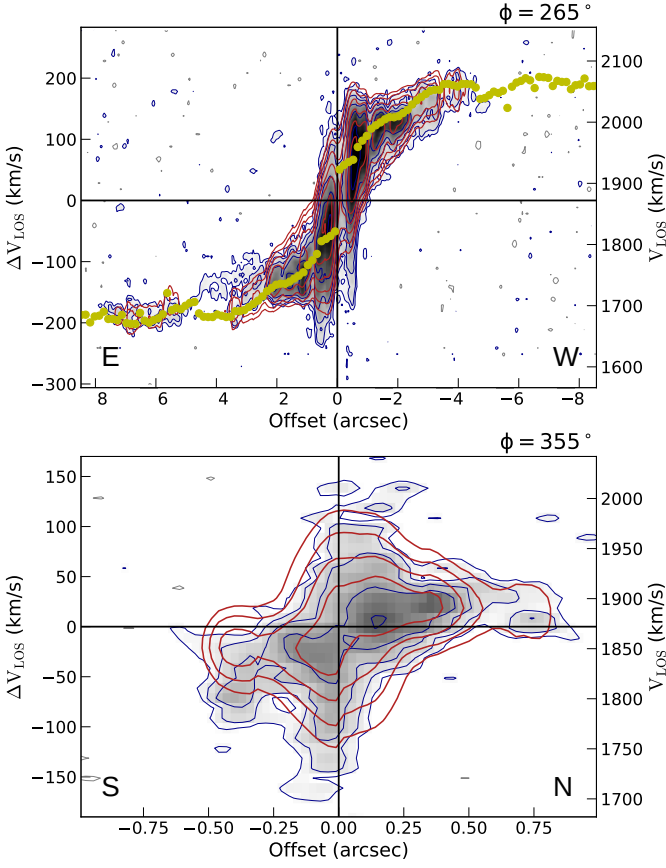


Fig. 6. Same as Fig. 4, but for the 3DB run with a radial velocity component.

radial motions associated with molecular inflows or outflows. Fig. 4 displays the position-velocity (PV) diagrams resulting from this run. Overall, the 3DB model contours (red lines in Fig. 4) reasonably reproduce the observed PV values (plotted with blue colours). From the major-axis PV diagram (Fig. 4, top panel) we can appreciate the goodness of the  $v_{\text{sys}}$  estimate, as the CO(3 – 2) emission is symmetric with respect to  $v_{\text{sys}}$ . Along the kinematic minor axis (Fig. 4, bottom panel), there are indications of non-circular motions in the central  $1''$ , which we explore further in the next section.

#### 4.2. Rotating disc with a radial velocity component

Within the approximate inner (projected)  $1''$ , the minor axis PV diagram shows redshifted motions to the north of the AGN and blueshifted to the south (see top-left and bottom-right quadrants, respectively, of Fig. 4, bottom panel). Since the south is the near side of the galaxy (see Fig. 3 and related discussion in Section 3.2), this suggests the presence of a CO outflow component in the plane of the disc. We thus run another 3DB model including a radial velocity ( $v_{\text{rad}}$ ) component. The other free parameters are  $v_{\text{rot}}$  and  $\sigma_{\text{gas}}$ , while the others have been set as the previous run.

Fig. 5 shows the 3DB models and residuals for this run, for the first and second moments (mean velocity and mean velocity dispersion). The velocity and velocity dispersion absolute residuals have median values of  $16 \text{ km s}^{-1}$  and  $14 \text{ km s}^{-1}$ , respectively. The highest velocity residuals (Fig. 5, second panel) are in the SE direction, where also the highest values of dispersion

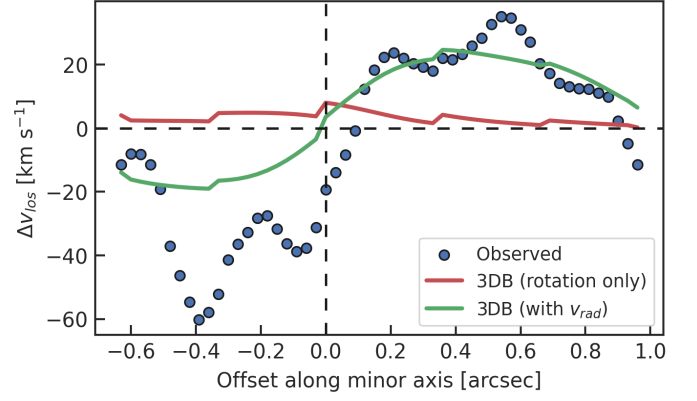


Fig. 7. Relative velocities of CO(3 – 2) along the minor axis, extracted and averaged from a slit width of 3 pixels (corresponding to a projected width of  $0.09''$ ). The blue circles are the observed values, not weighted for the emitted flux. The green and red lines are the 3DB models with and without a radial velocity component.

(Fig. 1, bottom panel) and dispersion residuals (Fig. 5, fourth panel) reside.

Fig. 6 shows the PV diagrams of this run, where we can appreciate a better fit along the minor axis (Fig. 6, bottom panel). Especially, the 3DB model now follows the northern red - southern blue asymmetry along the CO(3 – 2) minor axis. We also plot the mean velocities along the minor axis in Fig. 7, where we compare the 3DB results for the two models (with and without the radial velocity component). While not perfect, the model incorporating  $v_{\text{rad}}$  more closely aligns with the observed data, particularly at positive offsets from the centre (i.e. in the northern direction). The yellow dots in the top panel represent the mean  $v_{\text{rot}}$  (also plotted in the second panel of Fig. 8). We find  $v_{\text{rot}}$  reaching  $193 \text{ km s}^{-1}$  at  $r = 3.5''$  ( $440 \text{ pc}$ ), in reasonable agreement with the rotational velocity of  $181 \pm 5 \text{ km s}^{-1}$  measured from HI absorption (Gallimore et al. 1999).

The four panels in Fig. 8 show, from top to bottom, the CO(3 – 2) surface density  $\Sigma_{\text{CO}(3-2)}$ , and the modelled rotational velocity  $v_{\text{rot}}$ , velocity dispersion  $\sigma_{\text{gas}}$ , and radial velocity  $v_{\text{out}}^{\text{mol}}$  (which is the same as  $v_{\text{rad}}$ , with the positive sign meaning outflowing and negative meaning inflowing gas). We distinguish significant changes in the curve profiles at two particular radii:  $0.4''$  and  $5''$ .

At  $r \sim 0.4''$  ( $50 \text{ pc}$ ) we find the maximum value of  $\Sigma_{\text{CO}(3-2)}$ , which corresponds to the inner radius of the ring. Within this radius  $v_{\text{out}}^{\text{mol}} < 0$ , which is indicative of inflowing gas: it could be an indication of AGN feeding from the molecular disc (see e.g. Combes 2021), but since we only have two radial points we could not confirm this finding. At  $r \sim 0.4''$  we also have a peak in the  $\sigma_{\text{gas}}$  and  $v_{\text{out}}^{\text{mol}}$  profiles: this means that the molecular ring is not only rotating, but also outflowing (as in NGC 1068, see García-Burillo et al. 2019).

At  $r \sim 5''$  ( $610 \text{ pc}$ ) there is another peak of  $\sigma_{\text{gas}}$ , and  $v_{\text{out}}^{\text{mol}}$  goes from positive to negative, suggesting a transition from outflow to inflow (García-Burillo et al. 2014, found a similar result for NGC 1068). However, at  $r > 5''$  there is a lot of oscillation between inflow and outflow, probably due to the small number of datapoints (see the asymmetry of the CO emission in Fig. 1), so we did not take into consideration these outer radii.

The CO(3 – 2) radial motion on the molecular plane could be explained with (i) inflowing/outflowing gas (García-Bernetete et al. 2021; Ramos Almeida et al. 2022) or (ii) elliptical orbits as-

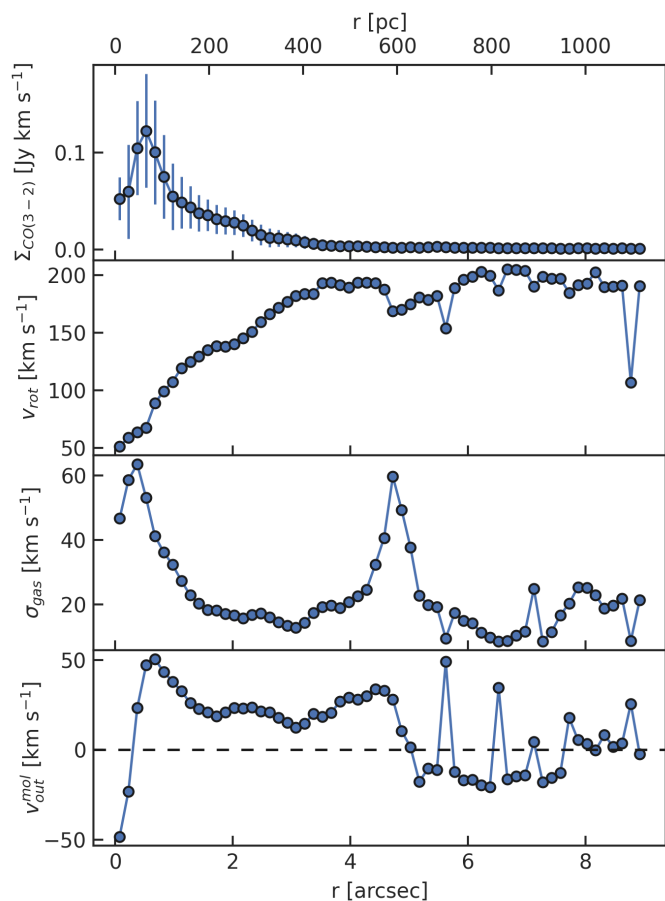


**Fig. 8.** Radial profiles of the molecular gas derived with 3DB. From top to bottom: the CO(3 – 2) surface density, the rotational velocity (same as the yellow dots in the top panel of Fig. 6), the velocity dispersion and the outflow velocity, all as a function of deprojected distance from the AGN (on the plane of the galaxy). The dashed black line in the bottom panel is the zero line, dividing between outflow ( $v_{\text{out}}^{\text{mol}} > 0$ ) and inflow ( $v_{\text{out}}^{\text{mol}} < 0$ ).

sociated with a bar (Buta & Combes 1996; Casasola et al. 2011; Audibert et al. 2019). Since the presence of a bar is not evident on the CO(3 – 2) PV diagrams (Figs. 4 and 6, cf. Alonso-Herrero et al. 2023), it probably does not dominate the motion of the molecular gas. Nevertheless, due to this possibility, we conservatively assume that the outflow velocities we derive between  $R_{\text{out},\text{min}}^{\text{mol}} = 0.4''$  (50 pc) and  $R_{\text{out},\text{max}}^{\text{mol}} = 5''$  (610 pc) are upper limits. We discuss the presence of a bar in NGC 5506 in Section 6.1.

#### 4.3. The molecular mass outflow rate

We used the CO(3 – 2) emission between  $R_{\text{out},\text{min}}^{\text{mol}} = 0.4''$  (50 pc) and  $R_{\text{out},\text{max}}^{\text{mol}} = 5''$  (610 pc) to calculate the main properties of the outflow, such as the amount of molecular gas it is driving outwards ( $M_{\text{out}}^{\text{mol}}$ ). To do so, we first converted it to CO(1 – 0), using a typical brightness temperatures ratio for galaxy discs of  $r_{31} \equiv T_{B,\text{CO}(3-2)}/T_{B,\text{CO}(1-0)} = 0.7$ : this is the average value found by Israel (2020) in 126 nearby galaxy centres, and we adopt it for consistency with García-Burillo et al. (2021). We then used a Galactic CO-to-H<sub>2</sub> conversion factor of  $X_{\text{CO}} = 2 \times 10^{20} \text{ mol cm}^{-2} (\text{K km s}^{-1})^{-1}$  (Bolatto et al. 2013). We chose the Galactic value to better compare our results with most of the literature, and also because NGC 5506 does not show any indication of merger and

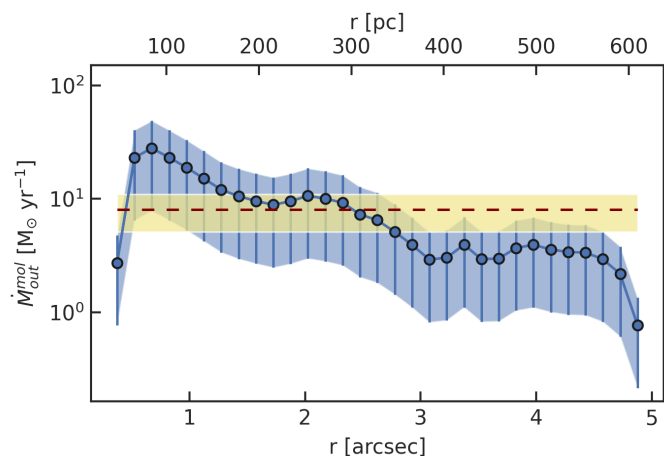


**Fig. 9.** Molecular gas mass outflow rate as a function of the deprojected distance from the AGN (on the plane of the galaxy). The molecular gas mass includes the helium contribution. The blue dots correspond to the values computed with the 3DB model radial velocities and CO(3 – 2) intensities of Fig. 8. The blue shading and errorbars represent the variation in  $r_{31}$  and  $X_{\text{CO}}$  (see text for details). The red dashed line is the integrated mass outflow rate,  $8 \pm 3 M_{\odot} \text{ yr}^{-1}$ , with the shaded yellow region representing its uncertainty.

is not particularly luminous in the infrared ( $L_{\text{IR}} = 10^{10.49} L_{\odot}$ , Sanders et al. 2003). We calculate  $M_{\text{out}}^{\text{mol}} = 1.75 \times 10^8 M_{\odot}$  between  $R_{\text{out},\text{min}}^{\text{mol}}$  and  $R_{\text{out},\text{max}}^{\text{mol}}$ . This result depends on our choice of  $r_{31}$  and  $X_{\text{CO}}$ . Specifically, a higher brightness temperatures ratio  $r_{31} \sim 1$ , as found in the central  $\sim 1''$  of NGC 1068 (García-Burillo et al. 2014; Viti et al. 2014), would decrease  $M_{\text{out}}^{\text{mol}}$ . Conversely, a lower  $r_{31} \sim 0.4$  (i.e. within  $1\sigma$  of the values collected by Israel 2020), would increase  $M_{\text{out}}^{\text{mol}}$ . Also a lower  $X_{\text{CO}} \sim 0.8 \times 10^{20} \text{ mol cm}^{-2} (\text{K km s}^{-1})^{-1}$ , usually associated to starburst galaxies (Bolatto et al. 2013; Pérez-Torres et al. 2021), would decrease  $M_{\text{out}}^{\text{mol}}$ . The combined uncertainty of these two conversions could decrease the calculated mass by a multiplicative factor of  $\approx 0.28$  or increase it by a factor of  $\approx 1.75$ .

Assuming a simple shell geometry (as in Alonso-Herrero et al. 2023), we can write the mass outflow rate as

$$\dot{M}_{\text{out}}^{\text{mol}} = \frac{M_{\text{out}}^{\text{mol}} v_{\text{out}}^{\text{mol}}}{R_{\text{out}}^{\text{mol}}}, \quad (1)$$

where  $v_{\text{out}}^{\text{mol}}$  is defined as the average velocity measured between  $R_{\text{out},\text{min}}^{\text{mol}}$  and  $R_{\text{out},\text{max}}^{\text{mol}}$ . By taking the standard deviation as its uncertainty, we find  $v_{\text{out}}^{\text{mol}} = 25.6 \pm 9.4 \text{ km s}^{-1}$ , from which we infer a molecular mass outflow rate of  $\dot{M}_{\text{out}}^{\text{mol}} = 8 \pm 3 M_{\odot} \text{ yr}^{-1}$  (which includes the helium contribution).

Fig. 9 shows the radial profile of the mass outflow rate, i.e. the same calculation of Equation 1 for every radial ring. To account for different  $r_{31}$  and  $X_{\text{CO}}$ , we plotted errorbars in Fig. 9 corresponding to the typical ranges  $r_{31} = 0.4 - 1$  and  $X_{\text{CO}} = (0.8 - 2) \times 10^{20} \text{ mol cm}^{-2} (\text{K km s}^{-1})^{-1}$ . We find a strong peak of  $\dot{M}_{\text{out}}^{\text{mol}}$  at the inner radius of the molecular ring ( $R \sim 85 \text{ pc}$ ), which is outflowing (while rotating) up to  $\dot{M}_{\text{out},\text{max}}^{\text{mol}} = 28 M_{\odot} \text{ yr}^{-1}$ . A second (minor) peak is visible around 250 pc ( $\sim 2''$ ), within which resides half of the molecular mass, and which corresponds to a small  $v_{\text{out}}$  peak (bottom panel of Fig. 8).

The average value of  $\dot{M}_{\text{out}}^{\text{mol}} = 8 \pm 3 M_{\odot} \text{ yr}^{-1}$  is similar to those of other local Seyferts, which range from  $\sim 1 M_{\odot} \text{ yr}^{-1}$  to a few tens of  $M_{\odot} \text{ yr}^{-1}$  (Combes et al. 2013; García-Burillo



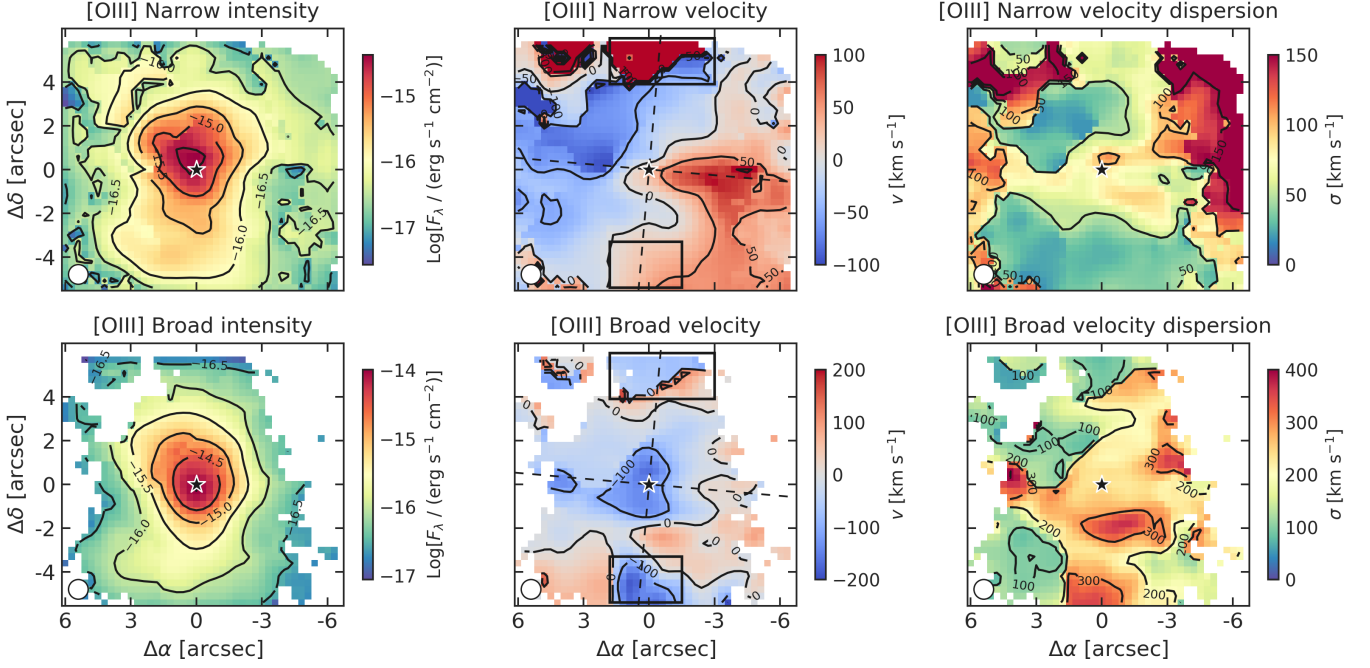


**Fig. 10.** [OIII] double Gaussian fit made with ALUCINE. Top and bottom rows are for the narrow and broad component, respectively. From left to right, the three columns show the intensity, velocity, and velocity dispersion of both components. The AGN position is marked with a black star symbol, and distances are measured from it. The white circle in the bottom left of each panel is the MEGARA seeing conditions. The velocity panels (central column) show the PA = 265° and 355° dashed black lines, and two black rectangles that highlight the northern and southern edges of the velocity field.

et al. 2014; Morganti et al. 2015; Alonso-Herrero et al. 2019; Domínguez-Fernández et al. 2020; García-Bernete et al. 2021; Alonso-Herrero et al. 2023).

## 5. Modelling the ionised gas kinematics

### 5.1. Gaussian decomposition

In the inset of Fig. 2 we presented the single Gaussian fit of the [OIII] line. It is evident that a single Gaussian cannot accurately reproduce the complex shape of the line profile. Consequently, we decided to fit the observed lines (listed in Fig. 2) with two Gaussians, spaxel by spaxel. The ALUCINE code determines, based on the  $\text{AoN} > 3$  cut, whether one or two Gaussians are necessary for each spaxel. As input parameters, ALUCINE needs also the wavelength range for subtracting the continuum, and a systemic velocity. At first we set  $v_{\text{sys,CO}} = 1872 \text{ km s}^{-1}$  as the CO(3–2), but we achieved better results by setting  $v_{\text{sys,[OIII]}} = 1893 \text{ km s}^{-1}$ . It is worth noting that this  $21 \text{ km s}^{-1}$  difference is only 1.5 times the MEGARA spectral step ( $\sim 14 \text{ km s}^{-1}$ ). A detailed comparison of  $v_{\text{sys}}$  values from the literature is available in Davies et al. (2020) and in Section 4.1.

We name the two Gaussians ‘narrow’ and ‘broad’ component, where their width is the discriminant factor. We focus mainly on the [OIII] line in the analysis, since it shows the highest signal (Fig. 2) and is the one usually studied for AGN ionised winds (Weedman 1970; Heckman et al. 1981; Veilleux 1991; Crenshaw & Kraemer 2000; Harrison et al. 2014). The results for the [OIII] line are in Fig. 10. The top panels show the narrow component: from the velocity map we can identify a rotation pattern, with velocities up to  $-100$  and  $100 \text{ km s}^{-1}$ , oriented roughly in the same way of the CO disc (Fig. 1). The external parts of the narrow component can be hardly associated to rotation however: at the northern end of the FoV the gas reaches  $340 \text{ km s}^{-1}$  (with

relatively low dispersions around  $60 \text{ km s}^{-1}$ ), while at NE and NW there are areas with very high dispersion (up to  $\sim 200 \text{ km s}^{-1}$ ). It could be that these extreme northern regions trace the external part of the ionised outflow.

The broad component of [OIII] (bottom panels of Fig. 10) contains fewer pixels than the narrow one, since for some spaxels a single Gaussian component was sufficient to obtain a proper modelling (or the broad Gaussian had  $\text{AoN} < 3$ ). The velocity map of this component displays a central blueshifted region (up to  $-170 \text{ km s}^{-1}$ ), and some positive and negative velocities all over the FoV. The velocity dispersion map reaches higher values than the narrow one (up to  $400 \text{ km s}^{-1}$ ).

The Gaussian decomposition made with ALUCINE is able to separate the [OIII] rotation from the outflow component (except for the extreme northern regions at high velocity or velocity dispersion). The same applies for the other emission lines in the MEGARA spectrum, for which the results are shown in Appendix B. Compared to [OIII], the narrow component intensity maps of [NII], [SII], and [OI] are more consistent with an ionised rotating disc (aligned with the HST and ALMA discs, i.e. with PA  $\sim 265^\circ$ ), while the broad component is more elongated on the north-south direction, (as [OIII], H $\alpha$  and H $\beta$ ). This north-south elongation is especially evident in the velocity dispersion of the broad components of [NII] and [SII] (Figs. B.3 and B.4).

We also show, in Appendix C, the Baldwin, Phillips, Terevich (BPT) diagrams (Baldwin et al. 1981; Veilleux & Osterbrock 1987; Kewley et al. 2001; Kauffmann et al. 2003) made with the same fitted lines. From such diagrams (Figs. C.1 – C.3) we can conclude that most of the observed central emission is due to the AGN activity rather than star formation, both for the narrow and broad components.

We explain how we used this decomposition to calculate the [OIII] mass of the broad component in Section 5.3. However, the velocities obtained with ALUCINE represent mean veloci-

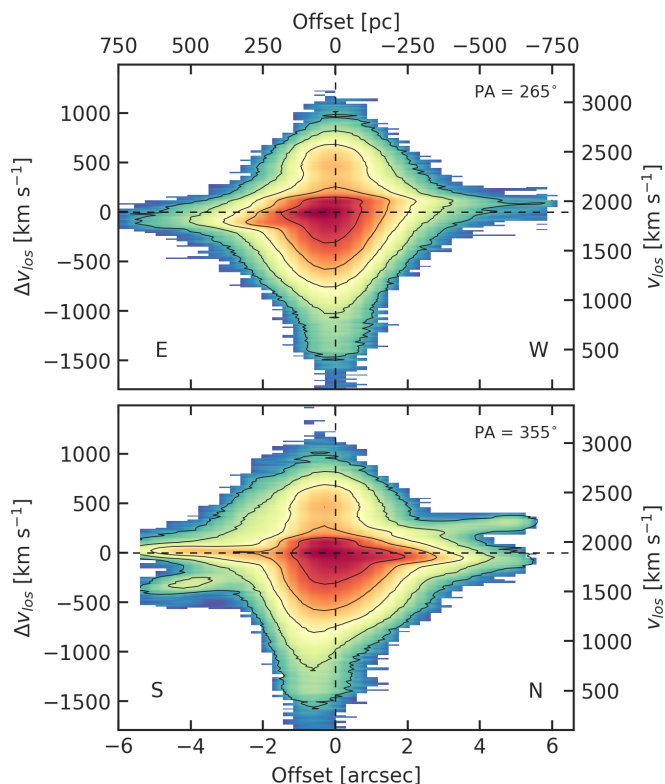


**Fig. 11.** PV diagrams of the observed [OIII] ( $\lambda_e = 5007\text{\AA}$ ) line, clipped at  $3\sigma$ , along major (*top panel*) and minor (*bottom panel*) kinematic axes, with PA =  $265^\circ$  and  $355^\circ$ , respectively. Contours are at  $[10, 30, 100, 300, 1000]\sigma$ . The vertical dashed line is the AGN position, and the horizontal dashed line is the systemic velocity  $v_{\text{sys}}^{\text{ion}} = 1893 \text{ km s}^{-1}$ . The approximate eastern, western, southern, and northern directions are marked in the panels. At  $\Delta v_{\text{los}} < -1500 \text{ km s}^{-1}$  contamination from the secondary [OIII] line ( $\lambda_e = 4959\text{\AA}$ ) is probable.

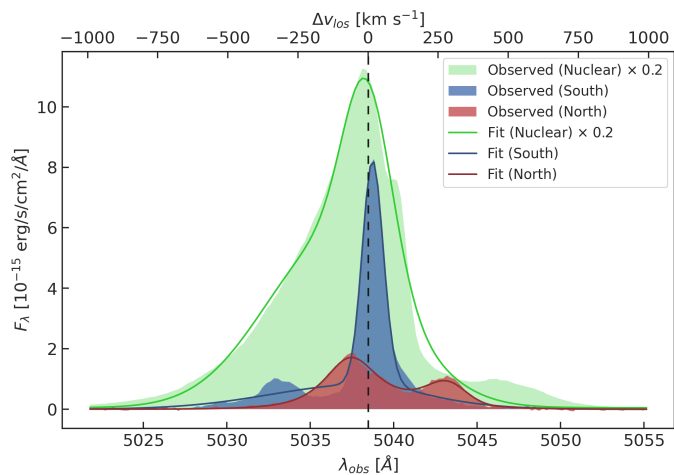


**Fig. 12.** Observed spectra (continuum-subtracted) of the [OIII] $\lambda 5007$  line at three locations along the kinematical minor axis (PA =  $355^\circ$ ). In green, blue, and red shadings, the spectra extracted within the nuclear region (black square in Fig. 2), the southern region, and the northern region (black rectangles in Fig. 10), respectively. With the same colours, the lines are the ALUCINE two-component fits for the same regions. Note that for the nuclear and southern regions a third component would be needed to fit the residual blueshifted and redshifted components, respectively. The nuclear spectrum is multiplied by a 0.2 factor for a better comparison. The vertical dashed line is the redshifted (with  $v_{\text{sys}}^{\text{ion}} = 1893 \text{ km s}^{-1}$ ) [OIII] line.

ties within each spaxel. To explore the full range of velocities of the ionised gas, we produced [OIII] PV diagrams (Fig. 11), along the same PAs as the CO emission (Fig. 6). In both major- and minor-axis PV diagrams, the ionised gas exhibits velocities exceeding  $1000 \text{ km s}^{-1}$ , both redshifted and blueshifted. The most extreme blueshifted velocities ( $\Delta v_{\text{los}} < -1500 \text{ km s}^{-1}$ ) are possibly contaminated with emission from the secondary [OIII] doublet line ( $\lambda_e = 4959 \text{\AA}$ ). The major-axis PV diagram (Fig. 11, top panel) displays a rotation curve between  $-100$  and  $100 \text{ km s}^{-1}$ . However, most of the emission, along both PAs, appears to be dominated by the outflowing gas. Along the minor axis (bottom panel of Fig. 11), there is also an observable X shape, elongated at large radii, likely due to the northern red and southern blue regions in the central panels of Fig. 10 (within the black rectangles). These regions may represent the locations where the outflow is emerging from the nuclear zone.

To have a better understanding of the observed PV diagrams, we show, in Fig. 12, the [OIII] line profile at three locations along the minor axis. The northern (in red) and southern (in blue) regions exhibit two distinct components: one travelling at approximately the systemic velocity, and the other outflowing at  $\sim \pm 300 \text{ km s}^{-1}$ . The southern blue emission also displays a stronger centred emission, which is evident in the PV diagram (Fig. 11, bottom panel) at  $\geq 4''$  south (while its northern counterpart is fainter). In the Gaussian decomposition (Fig. 10), the northern region with high redshifted velocities likely belongs to the outflowing and broad component rather than to the rotational/narrow one. However, the associated flux (and consequently, the ionised mass within it) is negligible in our analysis (see Section 5.3).

We note here that, even if several works allow three or more Gaussians to fit the emission of [OIII] in AGN with possible outflows (e.g Harrison et al. 2014; Dall’Agnol de Oliveira et al. 2021; Speranza et al. 2022; Hermosa Muñoz et al. 2023), we limited our analysis to two components to have a simpler interpretation of them: we associated the narrow component to the ionised gas rotation, and the broad one to the outflow. Adding more Gaussians to the ALUCINE fit would result in higher velocities and velocity dispersions for the broader components (but we refer to the next section for a better characterisation of the outflow velocities). However, such broader components would add a small contribution to the modelled flux (see Fig. A.1), hence to the outflow mass.

## 5.2. Non-parametric [OIII] velocities

In the previous section we saw that the ionised gas (traced by [OIII]) shows very high velocities probably due to an AGN wind. However, due to the complex line profiles, it is hard to see the different velocities from the Gaussian decomposition of Fig. 10. In this section, we make use of a non-parametric method to measure the outflow velocities.

We followed the method described by Harrison et al. (2014) to spatially resolve the velocities of the [OIII] emission line. This method uses the [OIII] line produced as the sum of the two fitted Gaussians (Section 5.1). For every spaxel we calculate the velocities corresponding to different percentiles to the flux contained in the modelled line profile, namely the velocities at the 2<sup>nd</sup>, 5<sup>th</sup>, 10<sup>th</sup>, 90<sup>th</sup>, 95<sup>th</sup>, and 98<sup>th</sup> percentiles, respectively called  $v_{02}$ ,  $v_{05}$ ,  $v_{10}$ ,  $v_{90}$ ,  $v_{95}$ , and  $v_{98}$ . We also calculate, for every spaxel, the velocity of the emission line peak  $v_p$ .

The results are illustrated in Fig. 13. The top-left panel shows  $v_p$ , which is similar to the velocity of the narrow component of

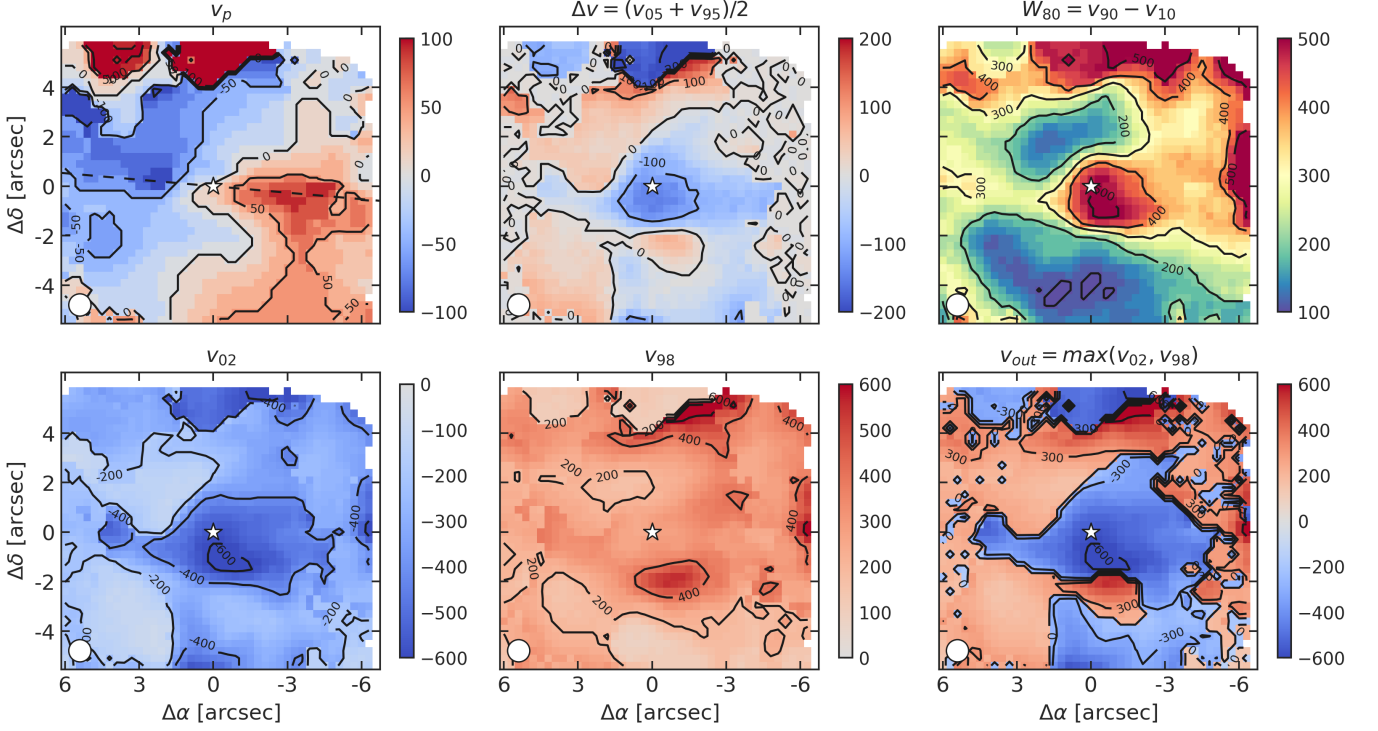


**Fig. 13.** Non-parametric velocity components for the [OIII] line. The top panels show, from left to right, the peak velocity  $v_p$ , the broad velocity  $\Delta v$ , and the 80% width  $W_{80}$ . The bottom panels show, from left to right, the velocity at the 2<sup>nd</sup> flux percentile ( $v_{02}$ ), at the 98<sup>th</sup> ( $v_{98}$ ), and the positive or negative velocities that have the maximum absolute value between these two (for every spaxel), which is our estimate for the outflow velocity  $v_{out}$ . The white star symbol marks the AGN position, and the dashed black line in the top-left panel is the kinematic major axis (PA = 265°). The white circle in the bottom left of each panel is the MEGARA seeing conditions. Velocities in all the panels are in km s<sup>-1</sup>.

the Gaussian decomposition (cf. Fig. 10). It has been shown that  $v_p$  traces the ionised gas rotation (Rupke & Veilleux 2013; Harrison et al. 2014). In the case of NGC 5506,  $v_p$  is similar to the mean-velocity field of the molecular gas, whose kinematic PA = 265° is plotted with a dashed black line. The region ~ 5'' N from the AGN, redshifted at ~ 300 km s<sup>-1</sup>, is not following the rotation pattern.

The top-central panel of Fig. 13 shows the  $\Delta v = (v_{05} + v_{95})/2$  map. This is very similar to the velocity map of the broad component modelled by ALUCINE (cf. Fig. 10), and so represents its velocity offset. There are differences between the two maps though, especially around ~ 3'' NE from the nucleus, where the  $\Delta v$  plot shows redshifted velocities around 50 km s<sup>-1</sup>. This may be an outflow feature lost in the ALUCINE decomposition map.

The top-right panel of Fig. 13 is the  $W_{80} = v_{90} - v_{10}$  width, which represents the width containing 80 percent of the [OIII] emitted flux. In the case of a single modelled Gaussian, this would correspond approximately to the FWHM. In our decomposition,  $W_{80}$  is, in a way, a combination of the velocity dispersions of the two components of Fig. 10. However,  $W_{80}$  exhibits larger values across the entire FoV, particularly at the AGN position (reaching up to 500 km s<sup>-1</sup>) and in the ~ 5'' N region (with an average  $\langle W_{80,N} \rangle \sim 500$  km s<sup>-1</sup>). The maximum value observed is  $W_{80,max} = 826$  km s<sup>-1</sup> located ~ 6'' W.

The bottom three panels of Fig. 13 show the velocities found in the 2<sup>nd</sup> and 98<sup>th</sup> percentiles of the flux (the third panel is showing the positive or negative velocities that have the maximum absolute value among the two). These correspond to the projected maximum values for the outflow velocities (as in Rupke & Veilleux 2013; Harrison et al. 2014; Davies et al. 2020). We find the highest blueshifted velocities around the AGN (–565 km s<sup>-1</sup>

at the AGN position, –620 km s<sup>-1</sup> at ~ 1'' S-SW) and in the ~ 5'' N region (up to –702 km s<sup>-1</sup>). The highest redshifted values are found at ~ 1.6'' (200 pc) S-SW from the AGN (up to 551 km s<sup>-1</sup>), and very close to the ~ 5'' N region (up to 689 km s<sup>-1</sup>).

The prevalence of blueshifted velocities in the nuclear region was previously identified in the X-shooter spectrum, extracted with a FoV of 1.8 × 1.8 arcsec<sup>2</sup> (Davies et al. 2020), which is also visible in Fig. 12 (green profile). With the MEGARA data, we observe high-velocity components, not associated with rotation, both blueshifted and redshifted, in all panels of Fig. 13 and in nearly every direction, particularly in the central 4 × 4 arcsec<sup>2</sup>, as evident in Fig. 11. This may be due to a wide bicone aperture, where any given line of sight intersects both approaching and receding clouds of gas simultaneously.

We isolate the [OIII] rotation velocity ( $v_{rot}$ ) by taking the median absolute value of  $v_p$  along the PA = 265° line (the dashed line in the  $v_p$  panel of Fig. 13) with a width of 4 pixels (corresponding to 1.2'' ~ 150 pc). In Fig. 14, we plot the mean radial profiles of  $v_{rot}$ ,  $\Delta v$ ,  $W_{80}$ , and  $v_{out}$ . The [OIII] rotational velocity  $v_{rot}$  flattens out at 83 km s<sup>-1</sup> around ~ 320 pc from the centre (Fig. 14, top panel), whereas the CO(3 – 2) flattens out at 193 km s<sup>-1</sup> around  $r = 440$  pc (Fig. 8, top panel). We point out that [OIII] is not the best tracer for the ionised disc rotation, and in fact it is the slowest rotator among the MEGARA lines: H $\alpha$  flattens at 120 km s<sup>-1</sup>, H $\beta$  at 113 km s<sup>-1</sup>, [NII] at 120 km s<sup>-1</sup>, [SII] at 118 km s<sup>-1</sup>, and [OI] at 110 km s<sup>-1</sup> (see Appendix D for the mean velocity radial profiles of all the MEGARA lines).

Interestingly, the ionised gas seems to be rotating at 60% the velocity of the molecular gas. Davis et al. (2013) found that, in CO-rich ATLAS<sup>3D</sup> galaxies (Cappellari et al. 2011), the difference between molecular and ionised rotation velocities was

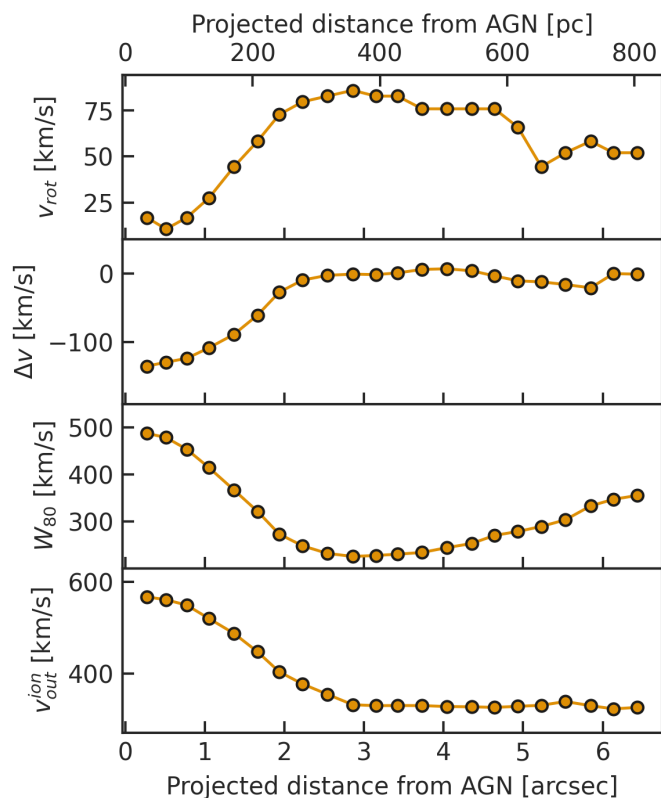


**Fig. 14.** Radial profiles for the different mean velocities of the [OIII] line, all as a function of the projected distance from the AGN. Panels show, from top to bottom: the rotational velocity  $v_{\text{rot}}$  along the kinematic axis, the broad velocity  $\Delta v$ , the 80% width  $W_{80}$ , and our estimate for the mean outflow velocity of the ionised gas  $v_{\text{out}}^{\text{ion}}$ .

larger for [OIII]-bright galaxies (up to a  $\Delta v_{\text{rot}} \sim 80 \text{ km s}^{-1}$ ), due to the different ionisation sources: a bright [OIII] emission (with respect to  $H\beta$ ) traces a dynamically hotter component of ionised gas than HII regions embedded in the cold star-forming disc. Also [Levy et al. \(2018\)](#) and [Su et al. \(2022\)](#) found the ionised gas to rotate slower than the molecular gas in EDGE-CALIFA ([Bolatto et al. 2017](#)) and ALMaQUEST ([Lin et al. 2019](#)) galaxies, but with a smaller difference of  $\sim 25 \text{ km s}^{-1}$ .

The radial profiles of  $\Delta v$ ,  $W_{80}$ , and  $v_{\text{out}}$  have similar shapes, with a smooth decrease of absolute velocities from the centre up to a radial distance of  $\sim 400 \text{ pc}$ . For these three quantities, the distance is the projected distance along every direction, so one has to be careful when comparing them to  $v_{\text{rot}}$  or to the molecular radial profiles of Figs. 8 and 9. We used the  $v_{\text{out}}$  radial profile of Fig. 14 to calculate the other ionised outflow properties, as the mass outflow rate (see Section 5.4).

### 5.3. The [OIII] outflow mass

In this section we calculate the electron density and mass of the ionised outflow. To do so, we make use of the ALUCINE decomposition (Section 5.1), and we consider the flux of the broad component as the outflow (whereas the narrow component is associated to the ordered gas rotation). We subsequently explain how we calculated the outflow properties using the [OIII] emission line (Fig. 10), but we also exploited the modelled broad components of  $H\alpha$ ,  $H\beta$ , and [NII] (Figs. B.1-B.3).

One of the challenges in the estimation of the ionised outflow mass is to properly calculate the gas volume density  $n$ , usually

expressed as the electron density  $n_e$  (where for ionised gas we expect  $n_e \sim n$ ). Many studies assume constant fiducial values for  $n_e$  (e.g. [Harrison et al. 2014](#); [Fiore et al. 2017](#)) for all the spaxels (or for a whole sample of galaxies). The most commonly used method to estimate  $n_e$  pixel-by-pixel is based on the [SII] doublet ratio ([Osterbrock & Ferland 2006](#)). However, this method has known biases, one of which is that the doublet ratio saturates above  $10^4 \text{ cm}^{-3}$ . We refer the interested reader to [Davies et al. \(2020\)](#) for a structured discussion on this topic and for a comparison between different methods to estimate  $n_e$ .

We follow [Baron & Netzer \(2019\)](#), [Davies et al. \(2020\)](#), and [Peralta de Arriba et al. \(2023\)](#), in estimating the ionised gas density from the ionisation parameter  $\log U$ , defined as the number of ionising photons per atom,  $U = Q_H / (4\pi r^2 n_H c)$ , where  $Q_H$  is the rate of hydrogen-ionising photons (in  $\text{s}^{-1}$  units),  $r$  is the distance from the ionising source,  $n_H \sim n_e$  is the hydrogen density, and  $c$  is the speed of light. Since  $Q_H$  can be estimated from the AGN bolometric luminosity ([Baron & Netzer 2019](#)), we can find  $n_e$  given the ionisation parameter.

Since the [OIII]/ $H\beta$  and [NII]/ $H\alpha$  line ratios are widely used in AGN studies ([Veilleux & Osterbrock 1987](#); [Kewley et al. 2001](#)), and both depend on  $\log U$ , [Baron & Netzer \(2019\)](#), by exploiting a sample of 234 type II AGN with outflow signatures, empirically determined (with a scatter of 0.1 dex) the following expression:

$$\log U = -3.766 + 0.191 \log\left(\frac{[\text{OIII}]}{H\beta}\right) + 0.778 \log^2\left(\frac{[\text{OIII}]}{H\beta}\right) - 0.251 \log\left(\frac{[\text{NII}]}{H\alpha}\right) + 0.342 \log^2\left(\frac{[\text{NII}]}{H\alpha}\right). \quad (2)$$

The resulting  $\log U$  map for the broad component of [OIII] is in the left panel of Fig. 15. There are fewer pixels than the broad [OIII] map (Fig. 10, bottom panels), since we had to use also the broad  $H\alpha$ ,  $H\beta$ , and [NII] maps, and only the pixels featured in all four maps are left (with  $H\beta$  being the most limiting one). We recover a median value of  $\log U = -2.9$ , in agreement with the integrated value of  $-2.87 \pm 0.12$  found by [Davies et al. \(2020\)](#) within the X-shooter FoV ( $1.8 \times 1.8 \text{ arcsec}^2$ ).

From the  $\log U$  definition, we follow [Baron & Netzer \(2019\)](#) and calculate the electron density as

$$n_e \approx 3.2 \left( \frac{L_{\text{bol}}}{10^{45} \text{ erg s}^{-1}} \right) \left( \frac{r}{1 \text{ kpc}} \right)^{-2} \left( \frac{1}{U} \right) \text{ cm}^{-3} \quad (3)$$

where we used the  $\log(L_{\text{bol}}/\text{erg s}^{-1}) = 44.1 \pm 0.09$  obtained by [Davies et al. \(2020\)](#) from the X-ray luminosity given by [Ricci et al. \(2017\)](#). For the central pixel we set  $r$  equal to half the pixel size.

We show the spatially resolved  $n_e$  map in the central panel of Fig. 15. We find  $n_e$  to decrease at increasing distance from the centre, as found by other works on local AGN (e.g. [Freitas et al. 2018](#); [Shimizu et al. 2019](#); [Davies et al. 2020](#); [Peralta de Arriba et al. 2023](#)). The maximum  $n_{e,\text{max}} = 8.5 \times 10^5 \text{ cm}^{-3}$  is exactly at the AGN position. To compare our values with the results of [Davies et al. \(2020\)](#) for NGC 5506, we calculate the median  $n_e$  at the edge of a  $1.8 \times 1.8 \text{ arcsec}^2$  FoV (the black square in Fig. 2), finding  $\log(n_e/\text{cm}^{-3}) = 3.95$ , which is very close to their integrated value of  $\log(n_e/\text{cm}^{-3}) = 4.03 \pm 0.14$ .

Before calculating the ionised outflow mass from the broad [OIII] luminosity, we have to correct it for the extinction. To do so, we assume an intrinsic ratio  $H\alpha/H\beta = 3.1$ , and we use the

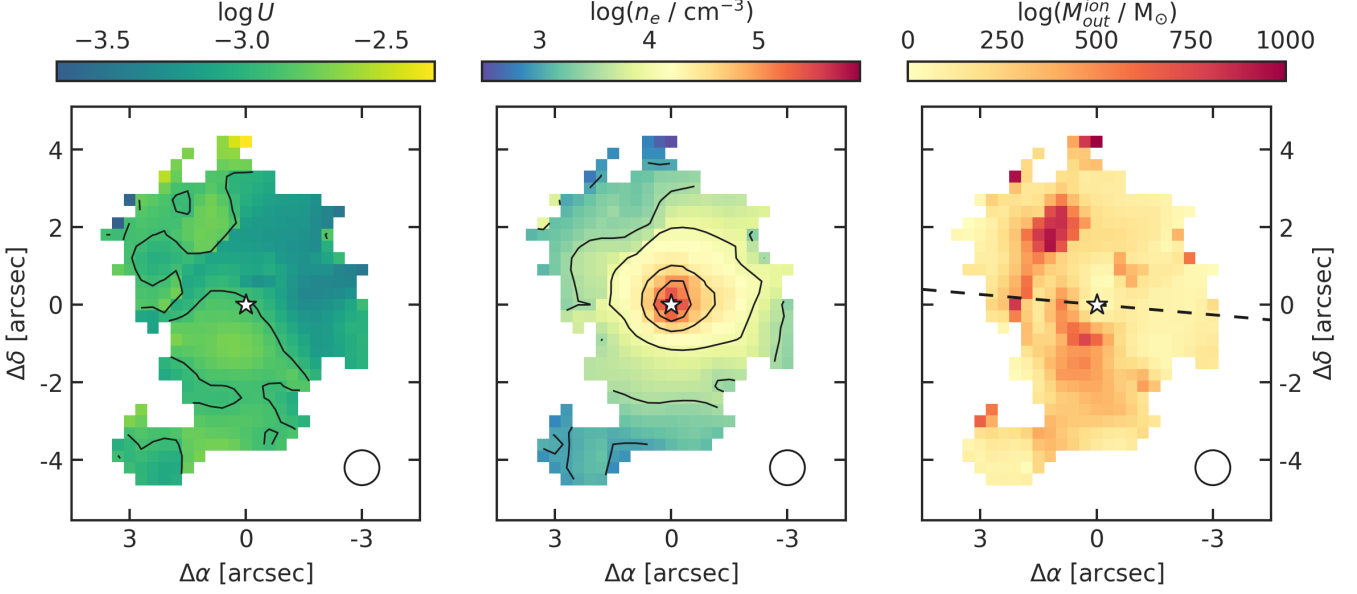


**Fig. 15.** From left to right: outflowing [OIII] ionisation parameter  $\log U$ , electron density  $n_e$ , and mass  $M_{\text{out}}^{\text{ion}}$ . Contours are at  $\log U = -2.9$  (i.e. its median value),  $\log(n_e \text{ cm}^{-3}) = (3, 3.5, 4, 4.5, 5)$ . The white star symbol marks the AGN position, and the dashed black line in the top-right panel is the kinematic major axis (PA = 265°). The white circle in the bottom right of each panel is the MEGARA seeing conditions.

Cardelli et al. (1989) extinction law ( $R_V = 3.1$ ). We find the [OIII] outflow area (i.e. the same of the three panels in Fig. 15) to have a median  $A_V = 1.9$  mag and an extinction-corrected total luminosity  $L_{\text{broad [OIII]}} = 10^{41.6}$  erg s $^{-1}$ . If we limit the FoV to  $1.8 \times 1.8$  arcsec $^2$  we find  $10^{41.3}$  erg s $^{-1}$ , in excellent agreement with the Davies et al. (2020) value of  $10^{41.2}$  erg s $^{-1}$ .

Finally, the ionised outflow mass  $M_{\text{out}}^{\text{ion}}$  is given by (see Rose et al. 2018; Baron & Netzer 2019):

$$M_{\text{out}}^{\text{ion}} = \frac{\mu m_H L_{\text{broad [OIII]}}}{\gamma_{\text{[OIII]}} n_e}, \quad (4)$$

where  $\mu = 1.4$  is the mean molecular weight,  $m_H$  is the hydrogen mass,  $L_{\text{broad [OIII]}}$  is the extinction-corrected broad [OIII] luminosity,  $n_e$  is the outflowing gas electron density, and  $\gamma_{\text{[OIII]}}$  is the effective line emissivity, which depends on the ionisation parameter (see Equations 5 and 6 in Baron & Netzer 2019). We interpolated the values listed in Baron & Netzer (2019), Table 2, to calculate  $\gamma_{\text{[OIII]}}$  for every spaxel.

The resulting spatial distribution of the outflowing [OIII] mass is presented in the right panel of Fig. 15. We calculated a total ionised outflowing mass of  $M_{\text{out}}^{\text{ion}} = 9.8 \times 10^4 M_{\odot}$ . In comparison, the mass reported by Davies et al. (2020) is  $3.2 \times 10^4 M_{\odot}$ . The discrepancy arises because the MEGARA aperture is significantly larger than the X-shooter one (as indicated by the white and black squares in Fig. 2). Additionally, Davies et al. (2020) used a single value for all the quantities involved in Equation 4, whereas we considered spatial variations, resulting in a more dispersed distribution of  $M_{\text{out}}^{\text{ion}}$ .

#### 5.4. The ionised mass outflow rate

We calculate the ionised mass outflow rate following, as for the molecular gas, Equation 1 (as in Rose et al. 2018; Baron & Netzer 2019; Davies et al. 2020). The outflow velocity and mass have been calculated following Sections 5.2 and 5.3. If we take, as typical outflow radius,  $R_{\text{out},95}^{\text{ion}} = 525$  pc (i.e. the one that contains 95% of  $M_{\text{out}}$ ), we find  $v_{\text{out}}^{\text{ion}} = 422 \pm 97$  km s $^{-1}$ , from which

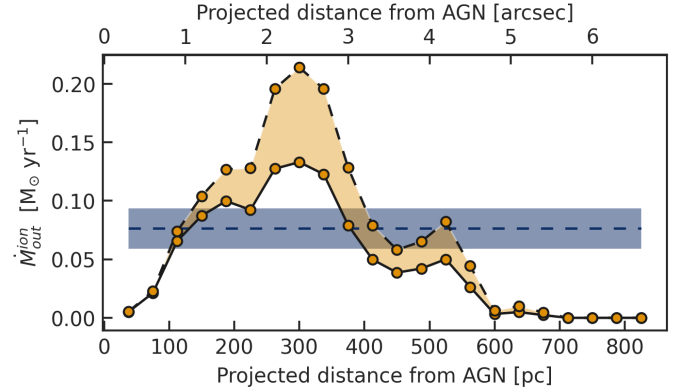


**Fig. 16.** Radial profile of the ionised mass outflow rate  $\dot{M}_{\text{out}}^{\text{ion}}$  as a function of the average projected distance from the AGN. Solid and dashed lines are estimates of  $\dot{M}_{\text{out}}^{\text{ion}}$  by using the average and the maximum  $v_{\text{out}}^{\text{ion}}$  at every radius. The blue dashed line is the integrated mass outflow rate,  $0.076 \pm 0.017 M_{\odot} \text{ yr}^{-1}$ , with the blue shading representing its uncertainty.

we infer a ionised mass outflow rate of  $\dot{M}_{\text{out}}^{\text{ion}} = 0.076 \pm 0.017 M_{\odot} \text{ yr}^{-1}$ , where the uncertainty comes from the standard deviation of the different measured radial velocities.

This is significantly lower than the  $0.21 M_{\odot} \text{ yr}^{-1}$  value reported in Davies et al. (2020). A factor of  $\sim 2$  discrepancy is due to the different velocity (they measured  $792$  km s $^{-1}$ ). Another difference is the outflow size, that dilutes the averaged value (their aperture radius was of  $117$  pc). We can recover the Davies et al. (2020) value if we plot the radial profile of  $\dot{M}_{\text{out}}$  (Fig. 16) using, for each radius, the maximum outflow velocity available (dashed black line) rather than the average one (solid black line).

The spatially resolved map of ionised mass outflow rate (Fig. 17) reveals an excess of  $\dot{M}_{\text{out}}^{\text{ion}}$ , extending from  $\sim 0.8''$  up to  $\sim 2.5''$  south of the AGN. This is the region where the most extreme blueshifted velocities of  $620$  km s $^{-1}$  reside (see Fig. 13). It is also a region which exhibit some excess of  $M_{\text{out}}$  (see Fig. 15,

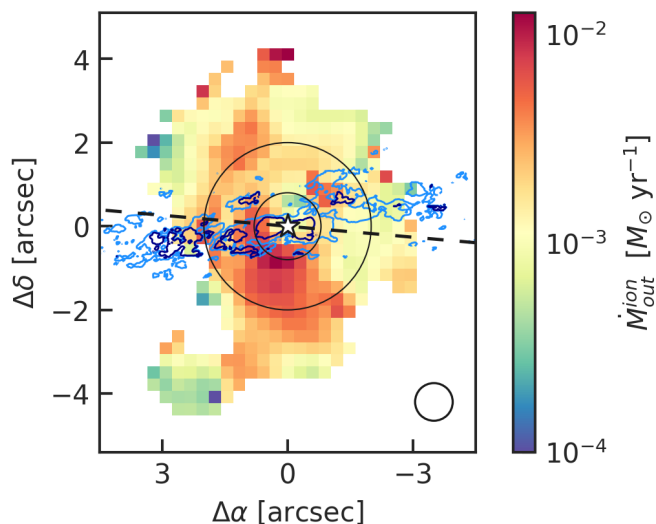


**Fig. 17.** Coloured map of the ionised mass outflow rate, with contours of observed CO(3–2) velocity dispersion (as Fig. 1, bottom panel), at 30 and 50 km s<sup>-1</sup> in light and dark blue, respectively. The two black circles have a radius of 100 and 250 pc (i.e.  $\sim 0.8$  and 2 arcsec, respectively) from the white star symbol, which marks the AGN position. The dashed line is the kinematic major axis. The white circle in the bottom right is the MEGARA seeing conditions.

right panel), hence the local high  $\dot{M}_{\text{out}}$ . Some minor  $\dot{M}_{\text{out}}$  clumps are visible at  $\sim 1.5''$  NW and  $\sim 2.5''$  NE from the AGN. Interestingly, this NE clump (which is very clear in the  $\dot{M}_{\text{out}}$  map) is located just after the separation between blueshifted and redshifted velocities (on the red side) in the bottom-left panel of Fig. 13. All together these clumps contribute to the two main bumps in the  $\dot{M}_{\text{out}}$  radial profile (Fig. 16).

The farthest (from the AGN) peak, at  $\sim 4'' \sim 500$  pc north, visible in both Fig. 16 and 17, is due to the pixels in the northern region highlighted in the central panels of Fig. 10, and whose spectrum is plotted in red in Fig. 12. Most of this northern region has been excluded from our analysis since it is out of the log  $U$  map (Fig. 15, left panel) and therefore of all the subsequent maps (this is mainly due to the limited size of the broad component of the H $\beta$  line, see Fig. B.2), but probably it is part of the ionised outflow. Interestingly, some molecular clouds are visible just north of the MEGARA FoV edge in Fig. 2.

Another region left out by Fig. 15 is the NW arc with high  $W_{80}$  values (Fig. 13), associated with LINER/shock emission in Figs. C.2 and C.3. This arc begins at the western edge of the CO(3–2) emission, but it may be linked to the high dispersion values we see going towards NW (bottom panel of Figs. 1 and 17). These two regions may indicate that the outflow (both in the ionised and molecular phases) has a larger size than the ones we derive with the present analysis. However, a more detailed mapping of the aforementioned areas is needed to draw meaningful conclusions.

The immediate vicinity of the AGN is relatively devoid of  $\dot{M}_{\text{out}}^{\text{ion}}$ , due to the small amount of  $\dot{M}_{\text{out}}^{\text{ion}}$  (see Fig. 15) in this region. This may stem from the observed ionised wind being a past outflow episode, now situated  $\sim 100$  pc from the centre, where it encounters resistance from the surrounding ISM. This corresponds to the same distance at which we observe a peak in the molecular mass outflow rate (Fig. 9), with the caveat that we are seeing projected distances for the ionised outflow, and deprojected distances (on the disc plane) for the molecular out-

flow. We subsequently compare the two phases in detail in the next section.

## 6. Discussion

### 6.1. The case for elliptical motions due to a bar

Being highly inclined, it is challenging to prove (or disprove) the presence of a bar in NGC 5506. *de Vaucouleurs et al. (1991)* classified this galaxy as a peculiar edge-on Sa, while *Baillard et al. (2011)*, by analysing SDSS images, signalled the presence of a "barely visible" stellar bar (with confidence ranging from "no bar" to "bar long about half  $D_{25}$ "). By inspecting PanSTARRS images we could in fact recognise an X-shape, typical of edge-on barred galaxies (*Baba et al. 2022*).

Edge-on barred galaxies typically display clearly separate components on the gas PV diagrams (see e.g. the compilation by *Bureau & Freeman 1999*). This is not evident on the molecular PV diagrams of NGC 5506 (Figs. 4 and 6), whereas instead it is noticeable on the major axis of NGC 7172 (*Alonso-Herrero et al. 2023*, Figs. 8 and 10), which is also a highly inclined galaxy. With the exception of the X-shape on the minor axis (explained in Section 5.1, see also Fig. 12), the same applies for the PV diagrams of the ionised gas (Fig. 11). This, however, could be to an unfavourable orientation of the bar, being too close to the minor axis to produce any apparent perturbation. It is also worth noting that NLSy1s as NGC 5506 are usually associated with the presence of a bar (*Crenshaw et al. 2003*).

The fact that we see disturbed molecular clouds on the north-west and south-east (Fig. 1, bottom panel), may be an indication of interaction of the ionised outflow with the molecular disc (Fig. 17). In the following section, we aim to provide a more comprehensive description of the interaction. However, it is important to note that we cannot rule out the potential existence of a bar within the central kiloparsec. Consequently, in our analysis of molecular inflow/outflow velocities (Fig. 8, bottom panel), we treat these results as upper limits.

### 6.2. Comparing molecular and ionised outflows

In Section 4 we modelled the ALMA CO(3–2) kinematics, finding a rotating disc along PA = 265°, within which the gas is also outflowing. The most intense region of the molecular outflow is at  $r \sim 100$  pc, with  $v_{\text{out,max}}^{\text{mol}} = 50$  km s<sup>-1</sup> and  $\dot{M}_{\text{out,max}}^{\text{mol}} = 28$  M $_{\odot}$  yr<sup>-1</sup>. This is also where most of the molecular mass resides. Another region of interest is at  $r \sim 250$  pc, where we found a second, more modest, peak of  $\dot{M}_{\text{out}}^{\text{mol}}(250 \text{ pc}) = 11$  M $_{\odot}$  yr<sup>-1</sup>. We plotted the circles of radii 100 and 250 pc in Fig. 17. If we follow the PA = 265° dashed line on the eastern side, we find enhanced values of  $\dot{M}_{\text{out}}^{\text{ion}}$  at such radii. This could be an evidence of interaction between the ionised AGN wind and the molecular disc, where we are seeing perhaps two different outflow episodes, in which case, from the 150 pc distance between the episodes, we can calculate, given a 500 km s<sup>-1</sup> velocity, a  $\Delta t_{\text{out}} = 0.3$  Myr (similar to the AGN flickering timescale derived by *Schawinski et al. 2015*; *King & Nixon 2015*).

We can have a closer look at the interaction between the ionised and molecular gas by plotting the CO(3–2) dispersion contours against the ionised mass outflow rate map, as in Fig. 17: not only do the  $\dot{M}_{\text{out}}^{\text{ion}}$  regions at 100 and 250 pc east from the AGN correlate with high CO dispersion ( $\sigma_{\text{CO}} \geq 50$  km s<sup>-1</sup>), but also the region  $\sim 1.5''$  NW has both a local excess of  $\dot{M}_{\text{out}}^{\text{ion}}$  and high  $\sigma_{\text{CO}}$  (up to 61 km s<sup>-1</sup>). From Fig. 17 (but also from Fig. 1)

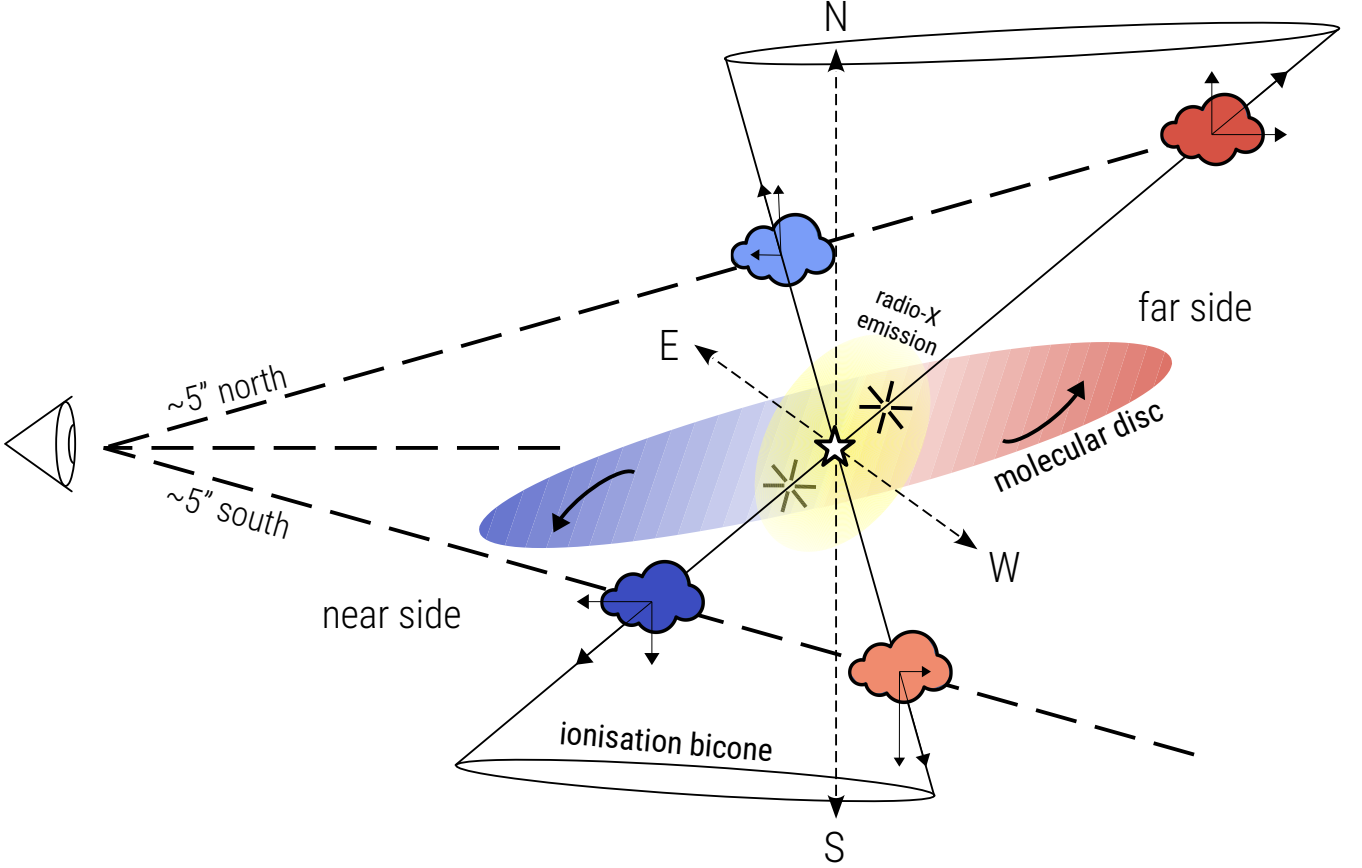


**Fig. 18.** Scenario (not to scale) for the intersection between the molecular disc (the red and blue ellipse) and the ionisation bicone. In the disc of the galaxy, traced by the molecular gas, we mark the AGN position (white star) and the proposed interactions between the two gas phases (black asterisk symbols). The 300-pc radius (at 8.46 GHz) and soft X-ray (below 1 keV) emission is depicted in yellow. Along the  $\pm 5''$  lines of sight, we draw clouds on the edge of the bicone, colour-coded depending on whether the gas is blueshifted or redshifted.

it seems NGC 5506 would be in the weak coupling scenario described by Ramos Almeida et al. (2022), i.e. where the biconical ionised outflow intercepts the molecular disc only partially, launching a modest molecular outflow (see also Alonso-Herrero et al. 2023). This would be in agreement with the bicone model fitted by Fischer et al. (2013) for NGC 5506: they found the inclination between the bicone and the host galaxy disc to be  $32^\circ$ , less than the maximum half-opening angle of the bicone ( $40^\circ$ , see Table 6 in Fischer et al. 2013).

We draw a tentative sketch of the relative positions of the molecular disc and the ionised bicone in Fig. 18. Every line of sight intercepts both approaching and receding sides of the bicone, resulting in a mix of blueshifted and redshifted velocities (as in Fig. 13). Once we are far enough from the disc plane ( $\sim 5''$  north and south), the edges of the bicone start to appear distinct on the spectra (Fig. 12): this would point out a hollow bicone. The southern nearest and northern farthest bicone edges intercept the molecular disc, hence rising the CO velocity dispersion and causing the molecular ring to outflow on the disc plane: this results in high CO dispersion on the SE-NW direction (Fig. 17), and in an asymmetry in the CO(3 – 2) PV diagram on the redshifted northern - blueshifted southern directions (Fig. 6, bottom panel).

An exception to the spatial correlation between  $\sigma_{CO}$  and  $\dot{M}_{out}^{ion}$  is in the immediate vicinity of the AGN: there the CO line broadening is probably due to the presence, in a small space, of multiple components of CO velocities, even due to ordered ro-

tation alone. Nevertheless, this region also has a deficit of CO emission (see Fig. 1 and García-Burillo et al. 2021), which may be another indication of multiphase feedback.

If we adopt the scenario drawn in Fig. 18, then the ionised outflow velocities we measured, especially the redshifted ones in the north and the blueshifted in the south, are lower limits due to projection effects. We did not perform a modelling of the bicone (so its opening angle in Fig. 18 is only qualitative), but if we adopt an half-opening angle of  $40^\circ$  (Fischer et al. 2013), we can derive a multiplicative factor of  $1/\sin(40^\circ) = 1.56$ , which would result in an average deprojected  $v_{out}^{ion} = 657 \pm 151 \text{ km s}^{-1}$ . Being the deprojected  $R_{out}^{ion}$  affected in the same way, this would not change the  $\dot{M}_{out}^{ion}$ .

If the AGN wind seen with the [OIII] and the outflowing CO ring are physically connected, we expect the kinetic energy rate ( $\dot{E}_{out}$ ) or the momentum rate ( $\dot{P}_{out}$ ) to be conserved (see King & Pounds 2015, and references therein). These two quantities can be straightforwardly calculated as  $\dot{E}_{out} = \dot{M}_{out} v_{out}^2/2$  and  $\dot{P}_{out} = \dot{M}_{out} v_{out}$ . The values (listed in Table 2) point to a energy-driven rather than momentum-driven outflow (King & Pounds 2015; Veilleux et al. 2020): in such outflows, the momentum undergoes a boost (e.g. Veilleux et al. 2020; Longinotti et al. 2023), which in our case is  $\dot{P}_{mol}/\dot{P}_{ion} = 7$ . However, if we use the values derived by Davies et al. (2020) for the ionised outflow, the ratio of the momentum rates would be  $\sim 1.2$ , rather indicating a momentum-driven outflow. Given the observed  $L_{bol}$  and  $\lambda_{Edd}$  (see Table 1), a radiation pressure-driven wind would predict an

**Table 2.** Results for the molecular and ionised phases of the AGN outflow. The distance from the AGN  $R_{\text{out}}$  is in different directions for the two phases.

Property	Molecular	Ionised
$R_{\text{out}}$ [pc]	610	525
$v_{\text{out}}$ [km s $^{-1}$ ]	$26 \pm 9$	$422 \pm 97$
$\dot{M}_{\text{out}}$ [ $M_{\odot}$ ]	$1.7 \times 10^8$	$9.4 \times 10^4$
$\dot{M}_{\text{out}}$ [ $M_{\odot}$ yr $^{-1}$ ]	$8 \pm 3$	$0.08 \pm 0.02$
$\dot{E}_{\text{out}}$ [ $10^{39}$ erg s $^{-1}$ ]	$1.7 \pm 1$	$4.3 \pm 1.7$
$\dot{P}_{\text{out}}$ [ $10^{32}$ dyn]	$13.1 \pm 6.7$	$2.0 \pm 0.7$

**Notes.** Molecular  $v_{\text{out}}$ ,  $\dot{M}_{\text{out}}$ ,  $\dot{E}_{\text{out}}$ , and  $\dot{P}_{\text{out}}$  are upper limits, due to the possible presence of elliptical motions associated with a nuclear bar. All the ionised values (except  $\dot{M}_{\text{out}}$  and  $\dot{M}_{\text{out}}$ ) are lower limits, since  $R_{\text{out}}$  and  $v_{\text{out}}$  are projected (on the plane of the sky) measurements.

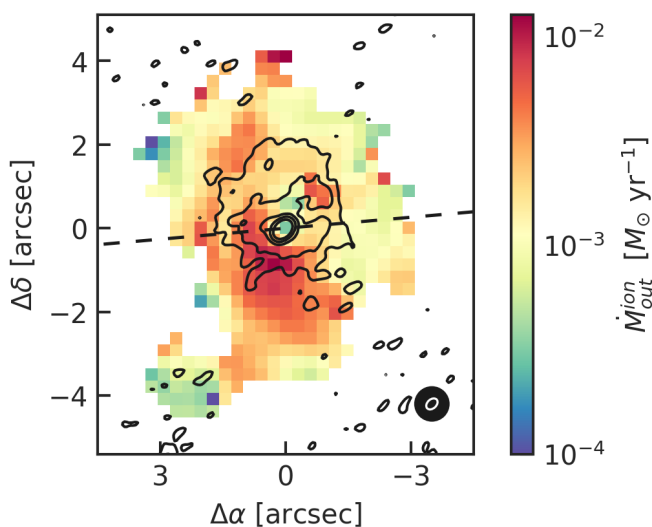


**Fig. 19.** Same as Fig. 17 but with the Schmitt et al. (2001) 3.6 cm VLA contours, at  $\log(S_{\nu}/Jy \text{ beam}^{-1}) = (-4, -3.5, -3, -2.5, -2)$ , in black. The black circle in the bottom right is the MEGARA seeing conditions, with the VLA beam ellipse within it in white.

outflow of  $\sim 3 M_{\odot} \text{ yr}^{-1}$  (Hönig 2019), not too far from our  $\dot{M}_{\text{out}}^{\text{mol}}$  value: this also would point to a momentum-driven scenario.

We highlight that the dichotomy between energy and momentum conservation refers to single or continuous outflow episodes. In the case of NGC 5506, we may be observing the stratification of multiple outflows, a possibility explored also in the next section. Taking everything into account, if the ionised wind is pushing and dragging the molecular gas, it currently seems to impact only the inner part of the molecular ring. At this stage, the AGN wind appears to be relatively ineffective in clearing the entire galaxy (which is common in local systems, see e.g. Fluetsch et al. 2019).

### 6.3. Extending the spectrum: radio and X-ray literature

Despite its classification as a radio-quiet galaxy (Terao et al. 2016), NGC 5506 has been detected in the radio band in several studies. Wehrle & Morris (1987) detected, with the VLA at 5 GHz, a radio bubble, NW from the nucleus, also visible in the 8.46 GHz VLA A-array continuum image presented by

Schmitt et al. (2001). In Fig. 19 we plot the contours of Schmitt et al. (2001) VLA image against the ionised mass outflow rate map, where we can see that the radio bubble observed by Wehrle & Morris (1987) perfectly overlaps with the  $\sim 1.5''$  region that has both high  $\dot{M}_{\text{out}}^{\text{ion}}$  and high  $\sigma_{\text{CO}}$ . The extended  $\sim 300$  pc VLA emission in Fig. 19 is well aligned with the galactic disc (PA =  $265^{\circ}$ ), but extends below and (mostly) over it, following the [OIII] emission. Orienti & Prieto (2010) measured, for this diffuse radio emission, a steep spectral index  $\alpha = 0.9$ , which combined with the size  $< 1$  kpc, would make it a compact steep spectrum (CSS) radio source (e.g. Dallacasa et al. 2013; O’Dea & Saikia 2021).

The VLA contours shown in Fig. 19 are also spatially coincident with the soft X-ray (below 1 keV) emission observed, with the Chandra X-ray Observatory, by Bianchi et al. (2003). Their main explanation is that the photoionised gas (that we clearly see with MEGARA, Fig. 2, even if more extended than 300 pc) is reprocessing the nuclear X-ray emission. However, since we detect velocities up to  $\sim 600$  km s $^{-1}$  out to 300 pc from the AGN, the expected temperature of the shocked emission is  $kT \approx 1.3(v_{\text{shock}}/10^3)^2$  keV  $\approx 0.5$  keV (Fornasini et al. 2022), which could suggest a thermal emission for the Chandra soft X-ray observation (see also Paggi et al. 2012).

High-resolution radio observations made with the Very Long Baseline Array (VLBA) at different frequencies (1.6 - 15 GHz, Roy et al. 2000), show a sub-relativistic ( $v_{\text{jet}} \leq 0.25c$ ) one-sided jet, initially oriented  $70^{\circ}$  anticlockwise from the north (so roughly as the CO disc), and then bending  $90^{\circ}$  towards the south (Kinney et al. 2000), at 3.4 pc ( $\sim 0.03''$ ) from the core emission. In Roy et al. (2001) they argue that the counterjet is not visible because of free-free absorption (rather than doppler boosting), and that the bend might be a sign of interaction between the jet and the NLR gas on parsec scales. Middelberg et al. (2004) collected different-epochs EVN, MERLIN and VLBA observations, and reported a  $3\sigma$  upper limit of  $0.50c$  for the jet motion with respect to the core. Gallimore et al. (2006) argue that the diffuse emission on the 300-pc scale (Fig. 19 and Schmitt et al. 2001), is attributed to the parsec-scale jet observed by Roy et al. (2000). The misalignment between the jet trajectory (initially pointing at  $\sim 70^{\circ}$  anticlockwise from north and later bending  $\sim 90^{\circ}$  towards the south) and the elongation of the diffuse radio emission towards the north direction can be explained by either jet precession or jet-ISM interactions (Gallimore et al. 2006, and also Xanthopoulos et al. 2010 come to the same conclusions).

Interestingly, such high velocities are also seen via absorption of the hard X-ray Fe XXVI Ly $\alpha$  line. The UFO in NGC 5506 has been observed and studied by Gofford et al. (2013) and Gofford et al. (2015), where they find  $v_{\text{UFO}} = 0.246 \pm 0.006 c$ . The momentum rate released by such a UFO ranges between  $5 \times 10^{33}$  and  $5 \times 10^{35}$  dyn, where this large uncertainty mostly comes from the estimation of the distance between the UFO and the AGN (see Tombesi et al. 2013, for a detailed derivation of the UFO parameters). Even the lower limit of  $\dot{P}_{\text{out}}^{\text{UFO}}$  is 3.8 times the molecular one (see Fig. 20). If we accept as good all these different measurements, a plausible explanation for this momentum decrease (instead of the boost required in the energy-driven scenario, or the constant  $\dot{P}_{\text{out}}$  in the momentum-driven scenario) is, again, that we are seeing different outflow episodes, among which the UFO is the most recent (also Sebastian et al. 2020, suggest multiple activity episodes for NGC 5506 from analysing polarised radio data). X-ray observations have shown in fact continuous rapid variation among different epochs (McHardy & Czerny 1987; Uttley & McHardy 2005; Sun et al. 2018), even sug-



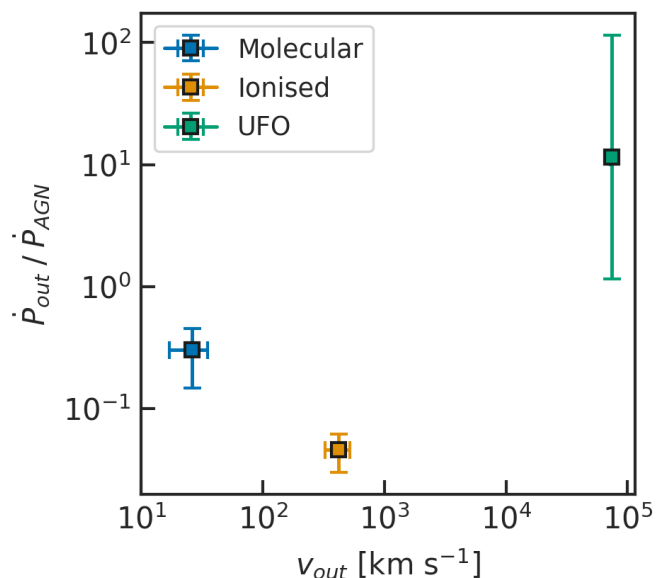


**Fig. 20.** Outflow momentum rate divided by the AGN radiation momentum rate  $L_{bol}/c$  (also called wind momentum load) as a function of the outflow velocity  $v_{out}$  for the molecular gas (in blue), the ionised gas (in orange), and the UFO (in green).

gesting the presence of a supermassive black hole binary system (Manchanda 2006).

Both relativistic jets (e.g. Mukherjee et al. 2018; Audibert et al. 2023, but also low-power jets, e.g. Venturi et al. 2021; Pereira-Santaella et al. 2022) and UFOs (e.g. Marasco et al. 2020; Longinotti et al. 2023; Salomé et al. 2023) are thought to be the initial trigger of galaxy-scale ionised and molecular outflows (see Singha et al. 2023, for a recent discussion). Another possibility is that the VLBI radio structures seen by Roy et al. (2000) are shock signatures left by the X-ray UFO (Longinotti et al. 2018).

## 7. Summary and conclusions

We presented new GTC/MEGARA optical IFU observations of NGC 5506, complemented with ALMA Band 7 observations of the CO(3 – 2) transition (García-Burillo et al. 2021). NGC 5506 is a nearby ( $D = 26$  Mpc) luminous ( $L_{bol} \sim 1.3 \times 10^{44}$  erg s $^{-1}$ ) Seyfert galaxy, part of the GATOS sample (García-Burillo et al. 2021; Alonso-Herrero et al. 2021). The angular resolution of the ALMA observation ( $0.21'' \times 0.13''$ ) allows us to probe regions on physical scales of  $\sim 25$  pc for the molecular gas. The GTC/MEGARA observation, with a seeing of  $0.9''$  (corresponding to  $\sim 113$  pc at the distance of NGC 5506), offers a spectral resolution enabling the analysis of velocities as low as  $\sim 14$  km s $^{-1}$ .

The CO(3 – 2) map reveals a highly inclined ( $i = 80^\circ$ ) cold molecular gas ring, symmetric up to a radius of  $3.5'' \sim 438$  pc, with an eastern tail extending up to a  $8'' \sim 1$  kpc radius. The cold molecular gas mass of the ring is  $\sim 2.3 \times 10^8 M_\odot$ , calculated assuming a brightness temperature ratio of  $T_{B,CO(3-2)}/T_{B,CO(1-0)} = 0.7$  and a Galactic CO-to-H $_2$  conversion factor. The CO(3 – 2) kinematics reveal a rotating disc, flattening at  $193$  km s $^{-1}$  around  $r = 440$  pc, with clear signatures of non-circular motions. A 3D BAROLO model of a rotating disc with a radial velocity component reproduces reasonably well the observed CO kinematics, interpreted as a rotating and outflowing molecular ring. Within

a  $0.4''$  radius, fitted radial velocities are directed towards the centre, potentially indicating AGN feeding, though this finding could not be confirmed since this radius is very close to the ALMA beam size. At larger radii, the radial velocity is directed outwards, decreasing from a maximum of  $50$  km s $^{-1}$  to an average of  $26$  km s $^{-1}$ . The maximum molecular outflow radius is  $610$  pc, within which we calculate an integrated molecular gas mass outflow rate of  $\sim 8 \pm 3 M_\odot$  yr $^{-1}$ .

We detected several bright emission lines in the MEGARA spectra, with [OIII] $\lambda 5007$  standing out as the brightest. The spatially resolved BPT diagnostic diagrams predominantly reveal Sy-like excitation, ruling out a significant contribution from star formation over a projected region of  $1.5$  kpc  $\times$   $1.4$  kpc. The [OIII] kinematics appear to be dominated by the outflowing gas. Nevertheless, we separated disc rotation from non-circular motion spaxel-by-spaxel, employing both parametric and non-parametric methods. The ionised gas exhibits a slower rotation speed than the molecular gas ( $\sim 190$  km s $^{-1}$ ), with H $\alpha$ , [NII] and [SII] reaching  $120$  km s $^{-1}$ . Conversely, we detected [OIII] radial velocities up to  $1000$  km s $^{-1}$ , both approaching and receding. Employing a non-parametric analysis of the line wings of [OIII] emission, we derived an average ionised gas outflow velocity of  $422$  km s $^{-1}$  within a radius of  $525$  pc. To estimate the outflowing mass, we utilised the broad component intensity maps from the double Gaussian decomposition. We calculated the electron density in every spaxel using the ionisation parameter method. This analysis yielded an outflowing mass of  $9.8 \times 10^4 M_\odot$ , resulting in an ionised mass outflow rate of  $\dot{M}_{out}^{ion} = 0.076 \pm 0.017 M_\odot$  yr $^{-1}$ .

We compared the spatially resolved map of  $\dot{M}_{out}^{ion}$  with the CO(3 – 2) velocity dispersion map, identifying spatial correlation between the two. The ionised outflow does not appear perpendicular to the plane of the galaxy; instead, it likely lies at a small angle relative to the disc. This results in a good geometrical coupling between the two phases. We also found diffuse radio and soft X-ray emission to spatially correlate with the observed [OIII] emission and  $\dot{M}_{out}^{ion}$ .

Various results, both from this study and the literature, suggest a diverse history of outflows for NGC 5506. These outflows may be associated with the presence of a parsec-scale radio jet, a  $0.25c$  UFO, or a combination of both. New ALMA and JWST observations, offering a higher resolution view of the nuclear region of NGC 5506, will soon become available as part of the GATOS project. These observations may eventually enhance our understanding of the complex interactions between the sub-parsec radio jet, the UFO, the ionised wind, and the molecular torus and disc.

*Acknowledgements.* We thank the anonymous referee for suggestions and comments that helped to improve the presentation of this work. We acknowledge the use of Python (Van Rossum & Drake 2009) and the following libraries: Astropy (Astropy Collaboration et al. 2013, 2018), CMasher (van der Velden 2020), Matplotlib (Hunter 2007), NumPy (Harris et al. 2020), Pandas (pandas development team 2020), pvextractor (Ginsburg et al. 2016), Seaborn (Waskom 2021), SciPy (Virtanen et al. 2020), and SpectralCube (Ginsburg et al. 2019). This research is based on observations made with the NASA/ESA Hubble Space Telescope obtained from the Space Telescope Science Institute, which is operated by the Association of Universities for Research in Astronomy, Inc., under NASA contract NAS 5–26555. These observations are associated with program 5479. This paper makes use of the following ALMA data: ADS/JAO.ALMA#2017.1.00082.S. ALMA is a partnership of ESO (representing its member states), NSF (USA) and NINS (Japan), together with NRC (Canada), MOST and ASIAA (Taiwan), and KASI (Republic of Korea), in cooperation with the Republic of Chile. The Joint ALMA Observatory is operated by ESO, AUI/NRAO and NAOJ. This research has made use of "Aladin sky atlas" developed at CDS, Strasbourg Observatory, France (Bonnarel et al. 2000). This research has made use of the NASA/IPAC Extragalactic Database (NED), which is funded by the National Aeronautics and Space Administration and operated by the California Institute of Technology. The authors acknowledge the use of computational resources from the paral-

lel computing cluster of the Open Physics Hub (<https://site.unibo.it/openphysicsclub/en>) at the Physics and Astronomy Department in Bologna. FE acknowledges support from grant PRIN MIUR 2017-20173ML3WW\_001, and funding from the INAF Mini Grant 2022 program "Face-to-Face with the Local Universe: ISM's Empowerment (LOCAL)". AAH and LHM acknowledge support from research grant PID2021-124665NB-I00 funded by MCIN/AEI/10.13039/501100011033 and by ERDF "A way of making Europe". SGB acknowledges support from the Spanish grant PID2022-138560NB-I00, funded by MCIN/AEI/10.13039/501100011033/FEDER, EU. IGB acknowledges support from STFC through grant ST/S000488/1 and ST/W000903/1. LPdA acknowledges financial support from grant PGC2018-094671-B-I00 funded by MCIN/AEI/10.13039/501100011033 and by ERDF "A way of making Europe". MPS acknowledges funding support from the Ramón y Cajal program of the Spanish Ministerio de Ciencia e Innovación (RYC2021-033094-I). CRA acknowledges support from EU H2020-MSCA-ITN-2019 Project 860744 "BID4BEST: Big Data applications for black hole Evolution Studies", from project "Feeding and feedback in active galaxies", with reference PID2019-106027GB-C42, funded by MICINN-AEI/10.13039/501100011033, and from project "Tracking active galactic nuclei feedback from parsec to kiloparsec scales", with reference PID2022-141105NB-I00. EB acknowledges the María Zambrano program of the Spanish Ministerio de Universidades funded by the Next Generation European Union and is also partly supported by grant RTI2018-096188-B-I00 funded by the Spanish Ministry of Science and Innovation/State Agency of Research MCIN/AEI/10.13039/501100011033. OGM acknowledges financial support from UNAM through the project PAPIIT IN109123 and from CONAHCYT through the project "Ciencia de Frontera 2023" CF-2023-G-100. CR acknowledges support from Fondecyt Regular grant 1230345 and ANID BASAL project FB210003.

## References

- Alexander, D. M. & Hickox, R. C. 2012, *New A Rev.*, 56, 93
- Alonso-Herrero, A., García-Burillo, S., Hönig, S. F., et al. 2021, *A&A*, 652, A99
- Alonso-Herrero, A., García-Burillo, S., Pereira-Santaella, M., et al. 2019, *A&A*, 628, A65
- Alonso-Herrero, A., García-Burillo, S., Pereira-Santaella, M., et al. 2023, *A&A*, 675, A88
- Alonso-Herrero, A., Pereira-Santaella, M., García-Burillo, S., et al. 2018, *ApJ*, 859, 144
- Anglés-Alcázar, D., Faucher-Giguère, C.-A., Quataert, E., et al. 2017, *MNRAS*, 472, L109
- Astropy Collaboration, Price-Whelan, A. M., Sipőcz, B. M., et al. 2018, *AJ*, 156, 123
- Astropy Collaboration, Robitaille, T. P., Tollerud, E. J., et al. 2013, *A&A*, 558, A33
- Audibert, A., Combes, F., García-Burillo, S., et al. 2019, *A&A*, 632, A33
- Audibert, A., Ramos Almeida, C., García-Burillo, S., et al. 2023, *A&A*, 671, L12
- Baba, J., Kawata, D., & Schönrich, R. 2022, *MNRAS*, 513, 2850
- Bacchini, C., Mingozi, M., Poggianti, B. M., et al. 2023, *ApJ*, 950, 24
- Baillard, A., Bertin, E., de Lapparent, V., et al. 2011, *A&A*, 532, A74
- Baldwin, J. A., Phillips, M. M., & Terlevich, R. 1981, *PASP*, 93, 5
- Baron, D. & Netzer, H. 2019, *MNRAS*, 486, 4290
- Baum, S. A. & McCarthy, P. J. 2000, *AJ*, 119, 2634
- Baumgartner, W. H., Tueller, J., Markwardt, C. B., et al. 2013, *ApJS*, 207, 19
- Bianchi, S., Balestra, I., Matt, G., Guainazzi, M., & Perola, G. C. 2003, *A&A*, 402, 141
- Bianchin, M., Riffel, R. A., Storchi-Bergmann, T., et al. 2022, *MNRAS*, 510, 639
- Bischetti, M., Piconcelli, E., Feruglio, C., et al. 2019, *A&A*, 628, A118
- Blustin, A. J., Page, M. J., Fuerst, S. V., Branduardi-Raymont, G., & Ashton, C. E. 2005, *A&A*, 431, 111
- Bolatto, A. D., Wolfire, M., & Leroy, A. K. 2013, *ARA&A*, 51, 207
- Bolatto, A. D., Wong, T., Utomo, D., et al. 2017, *ApJ*, 846, 159
- Bonnarel, F., Fernique, P., Bienaymé, O., et al. 2000, *A&AS*, 143, 33
- Bureau, M. & Freeman, K. C. 1999, *AJ*, 118, 126
- Buta, R. & Combes, F. 1996, *Fund. Cosmic Phys.*, 17, 95
- Cappellari, M., Emsellem, E., Krajnović, D., et al. 2011, *MNRAS*, 413, 813
- Cappi, M. 2006, *Astronomische Nachrichten*, 327, 1012
- Cardelli, J. A., Clayton, G. C., & Mathis, J. S. 1989, *ApJ*, 345, 245
- Carrasco, E., Gil de Paz, A., Gallego, J., et al. 2018, in *Society of Photo-Optical Instrumentation Engineers (SPIE) Conference Series*, Vol. 10702, Ground-based and Airborne Instrumentation for Astronomy VII, ed. C. J. Evans, L. Simard, & H. Takami, 1070216
- Casasola, V., Bianchi, S., De Vis, P., et al. 2020, *A&A*, 633, A100
- Casasola, V., Hunt, L. K., Combes, F., García-Burillo, S., & Neri, R. 2011, *A&A*, 527, A92
- Cicone, C., Brusa, M., Ramos Almeida, C., et al. 2018, *Nature Astronomy*, 2, 176
- Cicone, C., Maiolino, R., Sturm, E., et al. 2014, *A&A*, 562, A21
- Combes, F. 2021, in *Galaxy Evolution and Feedback across Different Environments*, ed. T. Storchi Bergmann, W. Forman, R. Overzier, & R. Riffel, Vol. 359, 312–317
- Combes, F., García-Burillo, S., Casasola, V., et al. 2013, *A&A*, 558, A124
- Cornachione, M. A., Morgan, C. W., Millon, M., et al. 2020, *ApJ*, 895, 125
- Crenshaw, D. M. & Kraemer, S. B. 2000, *ApJ*, 532, L101
- Crenshaw, D. M., Kraemer, S. B., & Gabel, J. R. 2003, *AJ*, 126, 1690
- Croton, D. J., Springel, V., White, S. D. M., et al. 2006, *MNRAS*, 365, 11
- Dabhade, P., Röttgering, H. J. A., Bagchi, J., et al. 2020, *A&A*, 635, A5
- Dallacasa, D., Orienti, M., Fanti, C., Fanti, R., & Stanghellini, C. 2013, *MNRAS*, 433, 147
- Dall'Agnol de Oliveira, B., Storchi-Bergmann, T., Kraemer, S. B., et al. 2021, *MNRAS*, 504, 3890
- Davies, R., Baron, D., Shimizu, T., et al. 2020, *MNRAS*, 498, 4150
- Davies, R. I., Maciejewski, W., Hicks, E. K. S., et al. 2014, *ApJ*, 792, 101
- Davis, T. A., Alatalo, K., Bureau, M., et al. 2013, *MNRAS*, 429, 534
- de Vaucouleurs, G., de Vaucouleurs, A., Corwin, Herold G., J., et al. 1991, *Third Reference Catalogue of Bright Galaxies*
- Di Teodoro, E. M. & Fraternali, F. 2015, *MNRAS*, 451, 3021
- Di Teodoro, E. M. & Peek, J. E. G. 2021, *ApJ*, 923, 220
- Domínguez-Fernández, A. J., Alonso-Herrero, A., García-Burillo, S., et al. 2020, *A&A*, 643, A127
- Dubois, Y., Peirani, S., Pichon, C., et al. 2016, *MNRAS*, 463, 3948
- Dultzin-Hacyan, D., Schuster, W. J., Parrao, L., et al. 1992, *AJ*, 103, 1769
- Esposito, F., Vallini, L., Pozzi, F., et al. 2024, *MNRAS*, 527, 8727
- Esposito, F., Vallini, L., Pozzi, F., et al. 2022, *MNRAS*, 512, 686
- Fabian, A. C. 2012, *ARA&A*, 50, 455
- Fabian, A. C., Sanders, J. S., Allen, S. W., et al. 2011, *MNRAS*, 418, 2154
- Faucher-Giguère, C.-A. & Quataert, E. 2012, *MNRAS*, 425, 605
- Feruglio, C., Fiore, F., Carniani, S., et al. 2015, *A&A*, 583, A99
- Feruglio, C., Maiolino, R., Piconcelli, E., et al. 2010, *A&A*, 518, L155
- Fiore, F., Feruglio, C., Shankar, F., et al. 2017, *A&A*, 601, A143
- Fischer, T. C., Crenshaw, D. M., Kraemer, S. B., & Schmitt, H. R. 2013, *ApJS*, 209, 1
- Fluetsch, A., Maiolino, R., Carniani, S., et al. 2021, *MNRAS*, 505, 5753
- Fluetsch, A., Maiolino, R., Carniani, S., et al. 2019, *MNRAS*, 483, 4586
- Fornasini, F. M., Elvis, M., Maksym, W. P., et al. 2022, *ApJ*, 931, 65
- Freitas, I. C., Riffel, R. A., Storchi-Bergmann, T., et al. 2018, *MNRAS*, 476, 2760
- Fukunura, K., Tombesi, F., Kazanas, D., et al. 2015, *ApJ*, 805, 17
- Gaibler, V., Khochfar, S., Krause, M., & Silk, J. 2012, *MNRAS*, 425, 438
- Gallimore, J. F., Axon, D. J., O'Dea, C. P., Baum, S. A., & Pedlar, A. 2006, *AJ*, 132, 546
- Gallimore, J. F., Baum, S. A., O'Dea, C. P., Pedlar, A., & Brinks, E. 1999, *ApJ*, 524, 684
- García-Bernete, I., Alonso-Herrero, A., García-Burillo, S., et al. 2021, *A&A*, 645, A21
- García-Bernete, I., Alonso-Herrero, A., Rigopoulou, D., et al. 2024, *A&A*, 681, L7
- García-Burillo, S., Alonso-Herrero, A., Ramos Almeida, C., et al. 2021, *A&A*, 652, A98
- García-Burillo, S., Combes, F., Ramos Almeida, C., et al. 2019, *A&A*, 632, A61
- García-Burillo, S., Combes, F., Usero, A., et al. 2014, *A&A*, 567, A125
- Gil de Paz, A., Carrasco, E., Gallego, J., et al. 2016, in *Society of Photo-Optical Instrumentation Engineers (SPIE) Conference Series*, Vol. 9908, Ground-based and Airborne Instrumentation for Astronomy VI, ed. C. J. Evans, L. Simard, & H. Takami, 99081K
- Ginsburg, A., Koch, E., Robitaille, T., et al. 2019, *radio-astro-tools/spectral-cube: v0.4.4*, Zenodo
- Ginsburg, A., Robitaille, T., & Beaumont, C. 2016, *pvextractor: Position-Velocity Diagram Extractor*, *Astrophysics Source Code Library*, record ascl:1608.010
- Giustini, M., Rodríguez Hidalgo, P., Reeves, J. N., et al. 2023, *A&A*, 679, A73
- Gofford, J., Reeves, J. N., McLaughlin, D. E., et al. 2015, *MNRAS*, 451, 4169
- Gofford, J., Reeves, J. N., Tombesi, F., et al. 2013, *MNRAS*, 430, 60
- Guo, W.-J., Li, Y.-R., Zhang, Z.-X., Ho, L. C., & Wang, J.-M. 2022, *ApJ*, 929, 19
- Harris, C. R., Millman, K. J., van der Walt, S. J., et al. 2020, *Nature*, 585, 357
- Harrison, C. M., Alexander, D. M., Mullaney, J. R., & Swinbank, A. M. 2014, *MNRAS*, 441, 3306
- Harrison, C. M., Costa, T., Tadhunter, C. N., et al. 2018, *Nature Astronomy*, 2, 198
- Heckman, T. M. & Best, P. N. 2014, *ARA&A*, 52, 589
- Heckman, T. M., Miley, G. K., van Breugel, W. J. M., & Butcher, H. R. 1981, *ApJ*, 247, 403
- Hermosa Muñoz, L., Cazzoli, S., Márquez, I., et al. 2023, *arXiv e-prints*, arXiv:2311.12552

- Hewett, P. C. & Foltz, C. B. 2003, *AJ*, 125, 1784
- Hönig, S. F. 2019, *ApJ*, 884, 171
- Hopkins, P. F. & Hernquist, L. 2006, *ApJS*, 166, 1
- Hunter, J. D. 2007, *Computing in Science & Engineering*, 9, 90
- Ishwara-Chandra, C. H. & Saikia, D. J. 1999, *MNRAS*, 309, 100
- Israel, F. P. 2020, *A&A*, 635, A131
- Jha, V. K., Joshi, R., Chand, H., et al. 2022, *MNRAS*, 511, 3005
- Karachentsev, I. D., Kudrya, Y. N., Karachentseva, V. E., & Mitronova, S. N. 2006, *Astrophysics*, 49, 450
- Kauffmann, G., Heckman, T. M., Tremonti, C., et al. 2003, *MNRAS*, 346, 1055
- Kewley, L. J., Dopita, M. A., Sutherland, R. S., Heisler, C. A., & Trevena, J. 2001, *ApJ*, 556, 121
- King, A. & Nixon, C. 2015, *MNRAS*, 453, L46
- King, A. & Pounds, K. 2015, *ARA&A*, 53, 115
- King, A. R., Pringle, J. E., West, R. G., & Livio, M. 2004, *MNRAS*, 348, 111
- Kinney, A. L., Schmitt, H. R., Clarke, C. J., et al. 2000, *ApJ*, 537, 152
- Kormendy, J. & Ho, L. C. 2013, *ARA&A*, 51, 511
- Krajinović, D., Cappellari, M., de Zeeuw, P. T., & Copin, Y. 2006, *MNRAS*, 366, 787
- Kuźmicz, A., Jamrozy, M., Bronarska, K., Janda-Boczar, K., & Saikia, D. J. 2018, *ApJS*, 238, 9
- Laha, S., Guainazzi, M., Dewangan, G. C., Chakravorty, S., & Kembhavi, A. K. 2014, *MNRAS*, 441, 2613
- Lamperti, I., Pereira-Santaella, M., Perna, M., et al. 2022, *A&A*, 668, A45
- Levy, R. C., Bolatto, A. D., Teuben, P., et al. 2018, *ApJ*, 860, 92
- Lin, L., Pan, H.-A., Ellison, S. L., et al. 2019, *ApJ*, 884, L33
- Liu, G., Zakamska, N. L., Greene, J. E., Nesvadba, N. P. H., & Liu, X. 2013, *MNRAS*, 436, 2576
- Longinotti, A. L., Salomé, Q., Feruglio, C., et al. 2023, *MNRAS*, 521, 2134
- Longinotti, A. L., Vega, O., Krongold, Y., et al. 2018, *ApJ*, 867, L11
- Maiolino, R., Stanga, R., Salvati, M., & Rodriguez Espinosa, J. M. 1994, *A&A*, 290, 40
- Malkan, M. A., Gorjian, V., & Tam, R. 1998, *ApJS*, 117, 25
- Maloney, P. R., Hollenbach, D. J., & Tielens, A. G. G. M. 1996, *ApJ*, 466, 561
- Manchanda, R. K. 2006, *Advances in Space Research*, 38, 1387
- Marasco, A., Cresci, G., Nardini, E., et al. 2020, *A&A*, 644, A15
- McCarthy, I. G., Schaye, J., Ponman, T. J., et al. 2010, *MNRAS*, 406, 822
- McCarthy, P. J., Baum, S. A., & Spinrad, H. 1996, *ApJS*, 106, 281
- McHardy, I. & Czerny, B. 1987, *Nature*, 325, 696
- McNamara, B. R. & Nulsen, P. E. J. 2012, *New Journal of Physics*, 14, 055023
- Middelberg, E., Roy, A. L., Nagar, N. M., et al. 2004, *A&A*, 417, 925
- Morganti, R., Oosterloo, T., Oonk, J. B. R., Frieswijk, W., & Tadhunter, C. 2015, *A&A*, 580, A1
- Mukherjee, D., Bicknell, G. V., Wagner, A. Y., Sutherland, R. S., & Silk, J. 2018, *MNRAS*, 479, 5544
- Mullaney, J. R., Alexander, D. M., Fine, S., et al. 2013, *MNRAS*, 433, 622
- Nagar, N. M., Oliva, E., Marconi, A., & Maiolino, R. 2002, *A&A*, 391, L21
- Nomura, M., Ohsuga, K., Takahashi, H. R., Wada, K., & Yoshida, T. 2016, *PASJ*, 68, 16
- O’Dea, C. P. & Saikia, D. J. 2021, *A&A Rev.*, 29, 3
- Okamoto, T., Eke, V. R., Frenk, C. S., & Jenkins, A. 2005, *MNRAS*, 363, 1299
- Orienti, M. & Prieto, M. A. 2010, *MNRAS*, 401, 2599
- Osterbrock, D. E. & Ferland, G. J. 2006, *Astrophysics of gaseous nebulae and active galactic nuclei*
- Paggi, A., Wang, J., Fabbiano, G., Elvis, M., & Karovska, M. 2012, *ApJ*, 756, 39
- pandas development team, T. 2020, *pandas-dev/pandas: Pandas*
- Pascual, S., Cardiel, N., Picazo-Sanchez, P., Castillo-Morales, A., & de Paz, A. G. 2021, *guaix-ucm/megaradrp: v0.11*
- Pasini, T., Brügggen, M., de Gasperin, F., et al. 2020, *MNRAS*, 497, 2163
- Peralta de Arriba, L., Alonso-Herrero, A., García-Burillo, S., et al. 2023, *A&A*, 675, A58
- Pereira-Santaella, M., Álvarez-Márquez, J., García-Bernete, I., et al. 2022, *A&A*, 665, L11
- Pérez-Torres, M., Mattila, S., Alonso-Herrero, A., Aalto, S., & Efstathiou, A. 2021, *A&A Rev.*, 29, 2
- Perna, M., Arribas, S., Catalán-Torrecilla, C., et al. 2020, *A&A*, 643, A139
- Pogge, R. W. 1988, *ApJ*, 328, 519
- Proga, D., Stone, J. M., & Kallman, T. R. 2000, *ApJ*, 543, 686
- Ramos Almeida, C., Bischetti, M., García-Burillo, S., et al. 2022, *A&A*, 658, A155
- Rankine, A. L., Hewett, P. C., Banerji, M., & Richards, G. T. 2020, *MNRAS*, 492, 4553
- Ricci, C., Trakhtenbrot, B., Koss, M. J., et al. 2017, *ApJS*, 233, 17
- Riffel, R. A., Storchi-Bergmann, T., Riffel, R., et al. 2021, *MNRAS*, 504, 3265
- Riffel, R. A., Storchi-Bergmann, T., Riffel, R., et al. 2017, *MNRAS*, 470, 992
- Rose, M., Tadhunter, C., Ramos Almeida, C., et al. 2018, *MNRAS*, 474, 128
- Roy, A. L., Ulvestad, J. S., Wilson, A. S., et al. 2000, in *Perspectives on Radio Astronomy: Science with Large Antenna Arrays*, ed. M. P. van Haarlem, 173
- Roy, A. L., Wrobel, J. M., Wilson, A. S., et al. 2001, in *Galaxies and their Constituents at the Highest Angular Resolutions*, ed. R. T. Schilizzi, Vol. 205, 70
- Ruiz, J. R., Crenshaw, D. M., Kraemer, S. B., et al. 2005, *AJ*, 129, 73
- Rupke, D. S. N. & Veilleux, S. 2013, *ApJ*, 768, 75
- Salomé, Q., Krongold, Y., Longinotti, A. L., et al. 2023, *MNRAS*, 524, 3130
- Sanders, D. B., Mazzarella, J. M., Kim, D. C., Surace, J. A., & Soifer, B. T. 2003, *AJ*, 126, 1607
- Schawinski, K., Koss, M., Berney, S., & Sartori, L. F. 2015, *MNRAS*, 451, 2517
- Schmitt, H. R., Donley, J. L., Antonucci, R. R. J., Hutchings, J. B., & Kinney, A. L. 2003, *ApJS*, 148, 327
- Schmitt, H. R., Ulvestad, J. S., Antonucci, R. R. J., & Kinney, A. L. 2001, *ApJS*, 132, 199
- Sebastian, B., Kharb, P., O’Dea, C. P., Gallimore, J. F., & Baum, S. A. 2020, *MNRAS*, 499, 334
- Shimizu, T. T., Davies, R. I., Lutz, D., et al. 2019, *MNRAS*, 490, 5860
- Singha, M., O’Dea, C. P., & Baum, S. A. 2023, *Galaxies*, 11, 85
- Speranza, G., Ramos Almeida, C., Acosta-Pulido, J. A., et al. 2024, *A&A*, 681, A63
- Speranza, G., Ramos Almeida, C., Acosta-Pulido, J. A., et al. 2022, *A&A*, 665, A55
- Su, Y.-C., Lin, L., Pan, H.-A., et al. 2022, *ApJ*, 934, 173
- Sun, S., Guainazzi, M., Ni, Q., et al. 2018, *MNRAS*, 478, 1900
- Tarchi, A., Castangia, P., Columbano, A., Panessa, F., & Braatz, J. A. 2011, *A&A*, 532, A125
- Terao, K., Nagao, T., Hashimoto, T., et al. 2016, *ApJ*, 833, 190
- Tombesi, F., Cappi, M., Reeves, J. N., et al. 2013, *MNRAS*, 430, 1102
- Tombesi, F., Cappi, M., Reeves, J. N., et al. 2010, *A&A*, 521, A57
- Uttley, P. & McHardy, I. M. 2005, *MNRAS*, 363, 586
- van der Velden, E. 2020, *The Journal of Open Source Software*, 5, 2004
- Van Rossum, G. & Drake, F. L. 2009, *Python 3 Reference Manual* (Scotts Valley, CA: CreateSpace)
- Veilleux, S. 1991, *ApJS*, 75, 383
- Veilleux, S., Maiolino, R., Bolatto, A. D., & Aalto, S. 2020, *A&A Rev.*, 28, 2
- Veilleux, S. & Osterbrock, D. E. 1987, *ApJS*, 63, 295
- Venturi, G., Cresci, G., Marconi, A., et al. 2021, *A&A*, 648, A17
- Virtanen, P., Gommers, R., Oliphant, T. E., et al. 2020, *Nature Methods*, 17, 261
- Viti, S., García-Burillo, S., Fuente, A., et al. 2014, *A&A*, 570, A28
- Wagner, S. J. & Witzel, A. 1995, *ARA&A*, 33, 163
- Waskom, M. L. 2021, *Journal of Open Source Software*, 6, 3021
- Weedman, D. W. 1970, *ApJ*, 159, 405
- Wehrle, A. E. & Morris, M. 1987, *ApJ*, 313, L43
- Weymann, R. J., Morris, S. L., Foltz, C. B., & Hewett, P. C. 1991, *ApJ*, 373, 23
- Wilson, A. S., Baldwin, J. A., & Ulvestad, J. S. 1985, *ApJ*, 291, 627
- Wilson, A. S., Braatz, J. A., Heckman, T. M., Krolik, J. H., & Miley, G. K. 1993, *ApJ*, 419, L61
- Wolfire, M. G., Vallini, L., & Chevance, M. 2022, *ARA&A*, 60, 247
- Xanthopoulos, E., Thean, A. H. C., Pedlar, A., & Richards, A. M. S. 2010, *MNRAS*, 404, 1966

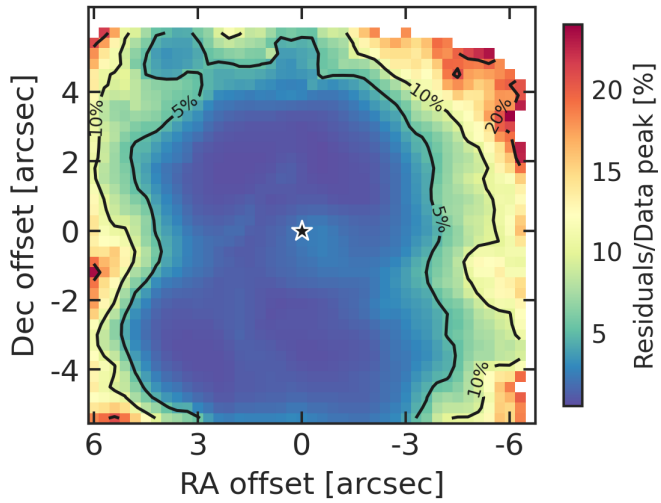


**Fig. A.1.** Residuals of the [OIII] ALUCINE fit (defined as  $|\text{observations} - \text{model}|$  divided by the observed peak flux, in every spaxel, in percentage).

### Appendix A: Goodness of ALUCINE fit

See Fig. A.1.

### Appendix B: Gaussian decomposition of MEGARA lines

See Figs. B.1, B.2, B.3, B.4, and B.5.

### Appendix C: BPT diagrams of MEGARA lines

See Figs. C.1, C.2 and C.3.

### Appendix D: Mean velocities radial profiles of all MEGARA lines

See Fig. D.1.

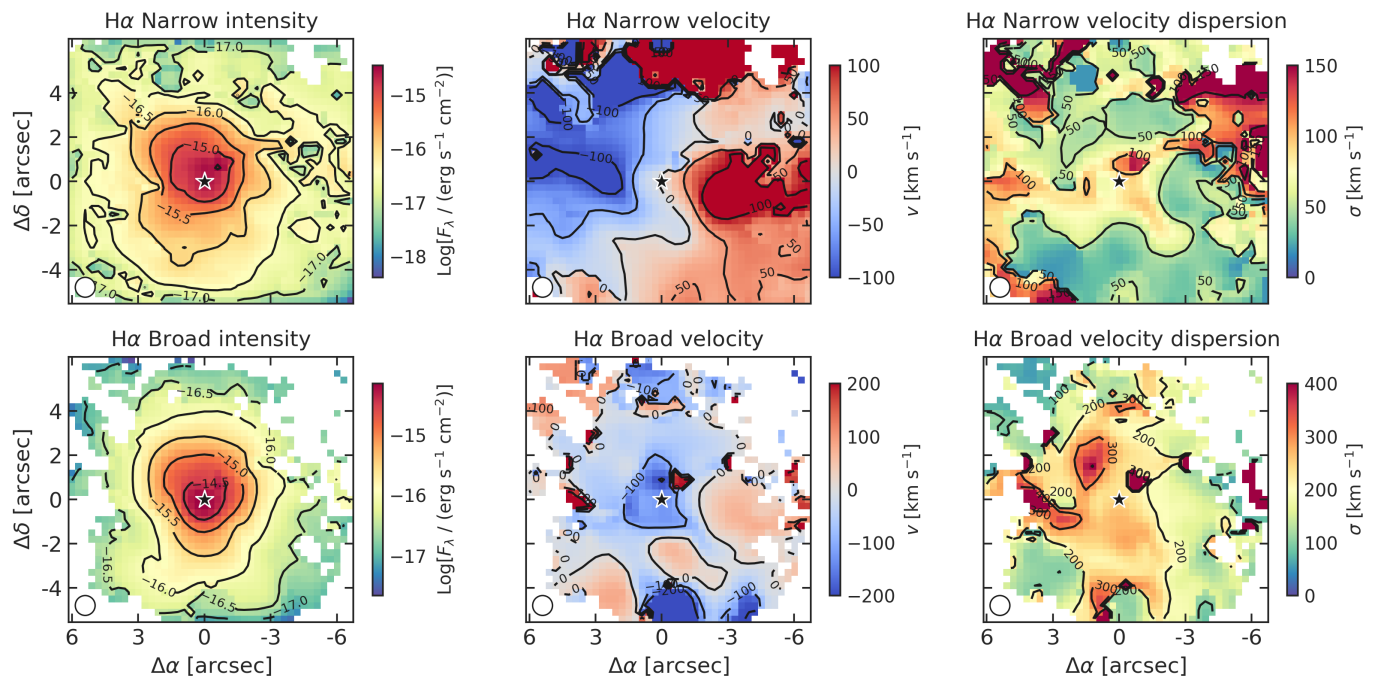


**Fig. B.1.** Gaussian decomposition made by ALUCINE for the  $H\alpha$  line. Top and bottom panels are for narrow and broad component, respectively, while in the three columns, from left to right, are the intensity, velocity, and velocity dispersion maps. The AGN position is marked with a black star symbol, and distances are measured from it. The white circle in the bottom left is the MEGARA seeing conditions.

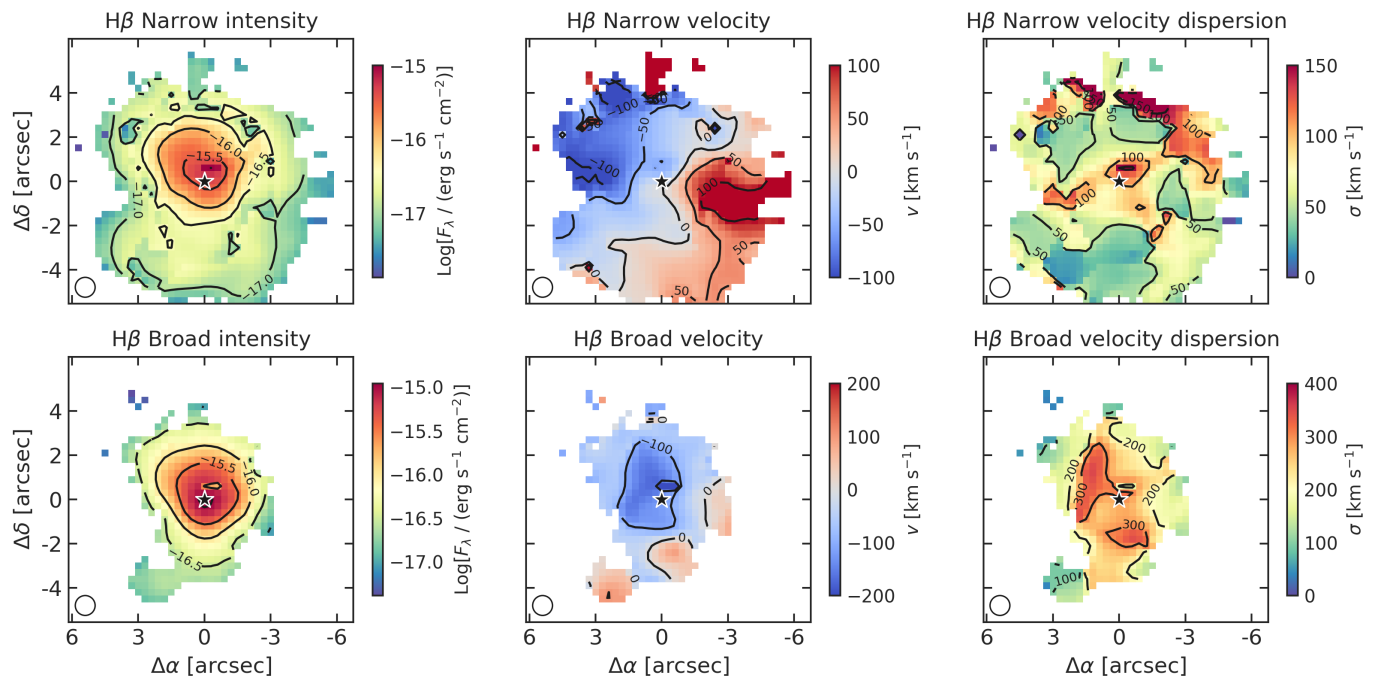


**Fig. B.2.** Same as Fig. B.1, but for the  $H\beta$  line.

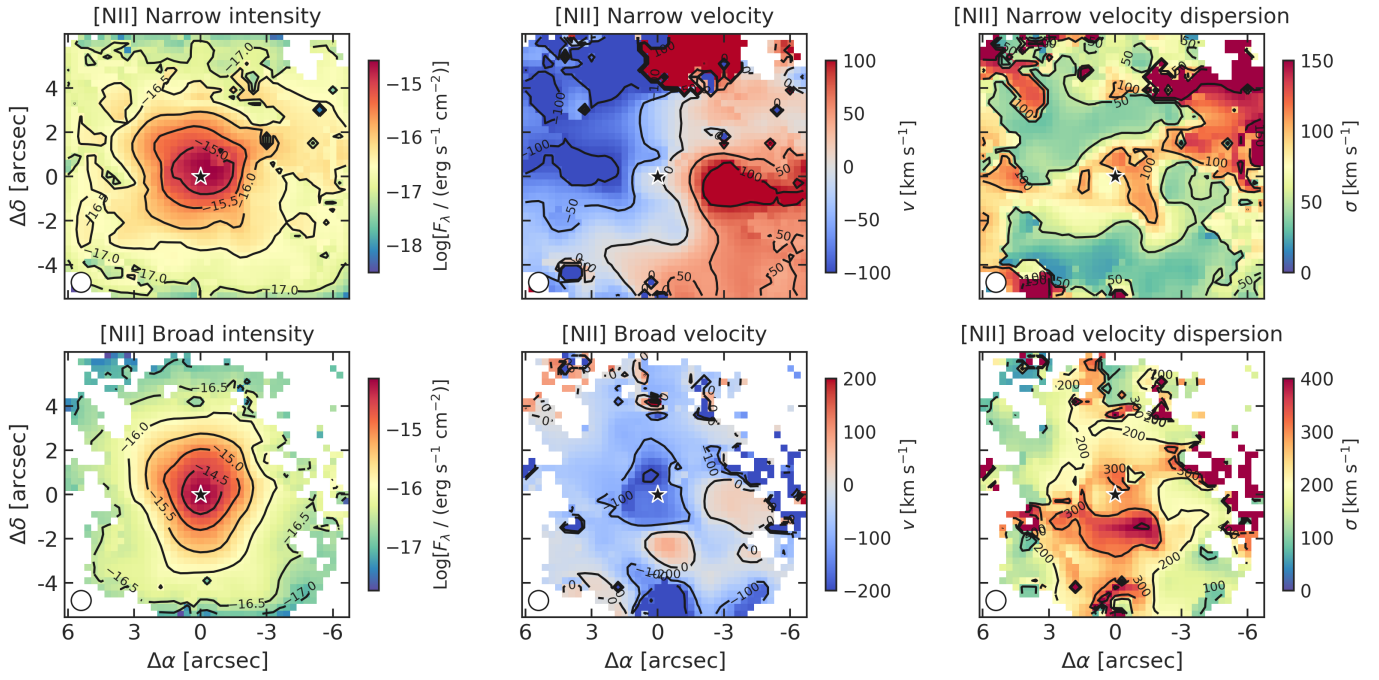


**Fig. B.3.** Same as Fig. B.1, but for the [NII] $\lambda\lambda 6548, 6583$  doublet. The intensity maps show the sum of the two lines of the doublet, while the kinematics are assumed to be the same between the two lines. The [NII] emission is fitted together with the blended H $\alpha$  line (Fig. B.1) to properly separate their kinematics.

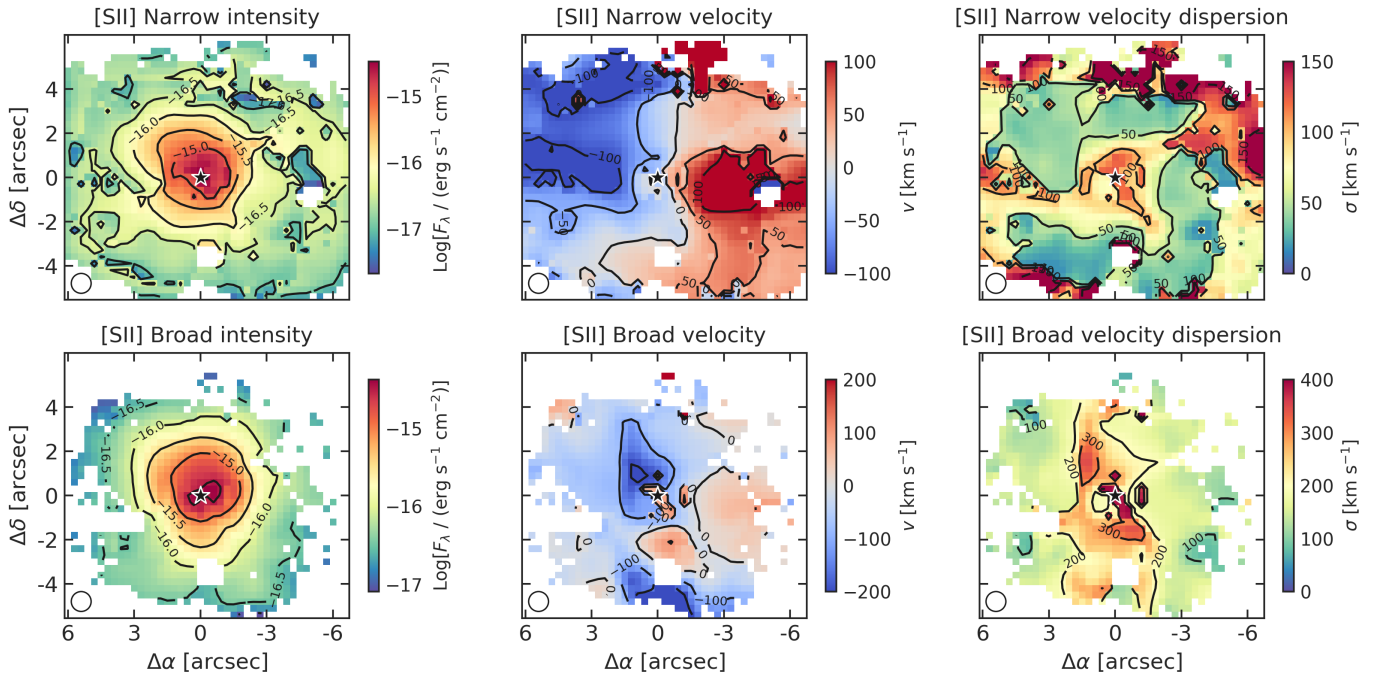


**Fig. B.4.** Same as Fig. B.1, but for the [SII] $\lambda\lambda 6716, 6731$  doublet. The intensity maps show the sum of the two lines of the doublet, while the kinematics are assumed to be the same between the two lines.

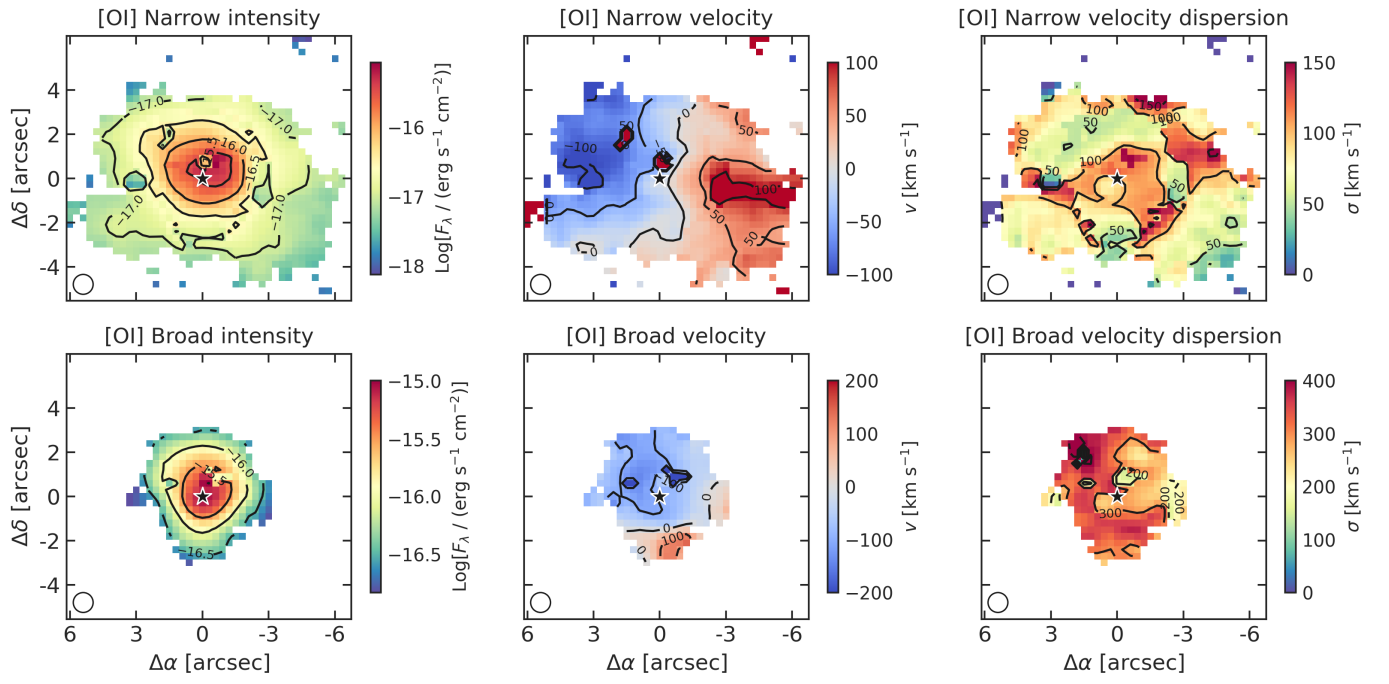


**Fig. B.5.** Same as Fig. B.1, but for the [OI] $\lambda 6300$  line.

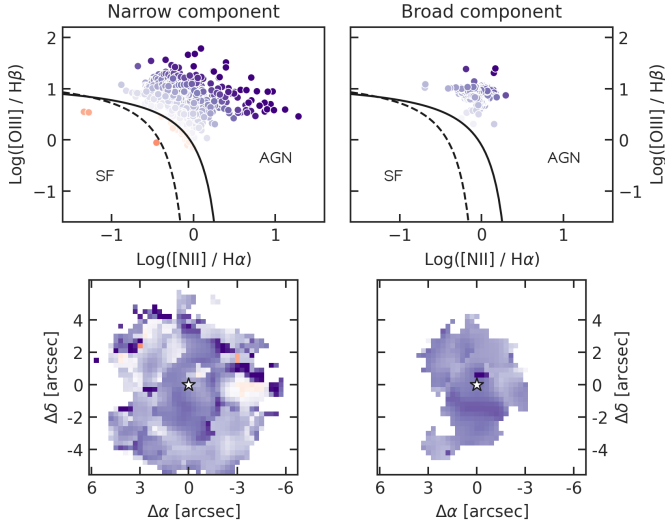


**Fig. C.1.** Diagnostic Baldwin, Phillips, Telervich (BPT) diagram (Baldwin et al. 1981; Veilleux & Osterbrock 1987) of  $[\text{OIII}]/\text{H}\beta$  vs  $[\text{NII}]/\text{H}\alpha$  line ratios, for the narrow (left panels) and broad (right panels) components of the ionised gas. Solid and dashed black lines are empirical curves derived by Kewley et al. (2001) and Kauffmann et al. (2003), that separate different excitation mechanisms, marked on the plots as SF (star formation) and AGN. The spaxels are coloured depending on their distance from the separation lines, and are plotted with the same colours in the spatially resolved maps (bottom panels). The black star marks the AGN position.

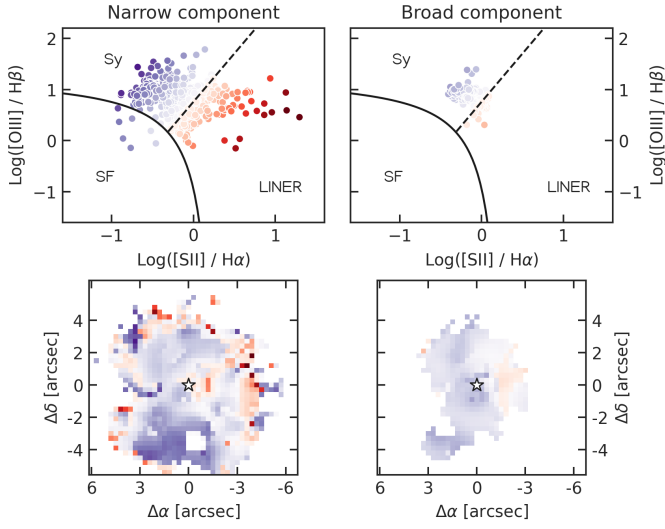


**Fig. C.2.** Same as Fig. C.1, but for the  $[\text{OIII}]/\text{H}\beta$  vs  $[\text{SII}]/\text{H}\alpha$ . The different excitation mechanisms are marked on the plots as SF (star formation), Sy (Seyfert), and LINER (low-ionisation nuclear emission-line region), with separation lines from Veilleux & Osterbrock (1987).

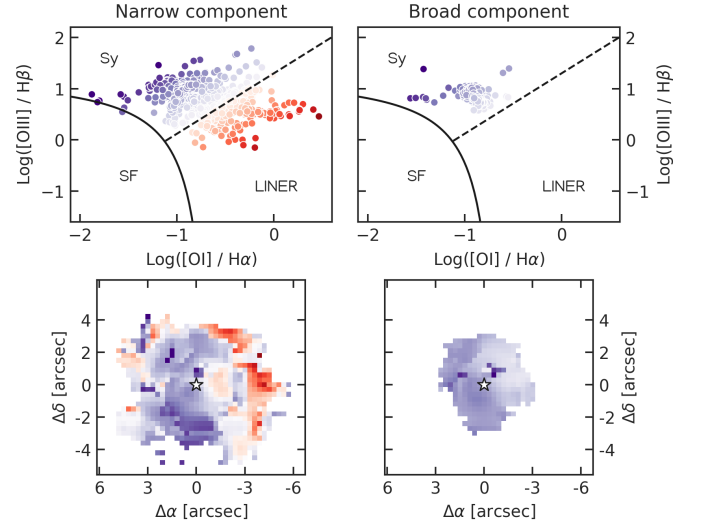


**Fig. C.3.** Same as Fig. C.1, but for the  $[\text{OIII}]/\text{H}\beta$  vs  $[\text{OI}]/\text{H}\alpha$ . The different excitation mechanisms are marked on the plots as SF (star formation), Sy (Seyfert), and LINER (low-ionisation nuclear emission-line region), with separation lines from Veilleux & Osterbrock (1987).

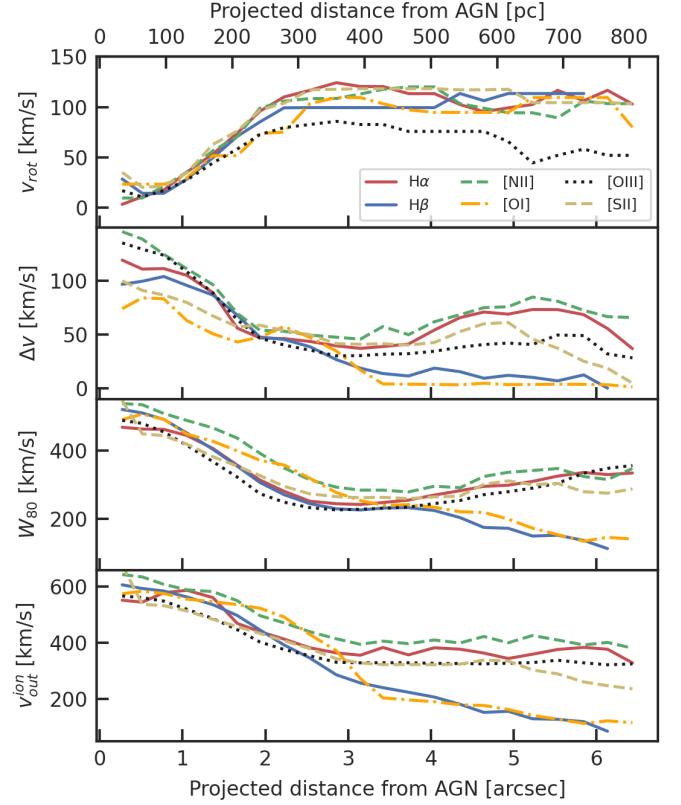


**Fig. D.1.** Same as Fig. 14, but for all the ionised gas emission lines.